

**Characterization of chirped photonic crystal fiber and its application in multiphoton
microscopy**

by

Jiali Yu

M.S., Huazhong University of Science and Technology, 2005

A THESIS SUBMITTED IN PARTIAL FULFILLMENT OF

THE REQUIREMENTS FOR THE DEGREE OF

MASTER OF APPLIED SCIENCE

in

THE FACULTY OF GRADUATE AND POSTDOCTORAL STUDIES

(Electrical and Computer Engineering)

THE UNIVERSITY OF BRITISH COLUMBIA

(Vancouver)

August 2013

© Jiali Yu, 2013

Abstract

Multiphoton Microscopy (MPM) is a widely used imaging technique in the biomedicine field by virtue of its subcellular resolution and biochemical specificity. Fiber-based multiphoton endoscopes are important for *in vivo* clinical application because they enable minimally invasive imaging. One major challenge for these endoscopes is the efficient delivery of ultrashort pulses in the near infrared region through the optical fibers. MPM requires ultrashort pulses to obtain high peak power for the nonlinear excitation. However, the optical components, especially the optical fibers, can introduce dispersion which can severely broaden the pulses and reduce the peak power. The purpose of this study is to find a good candidate of optical fibers that can propagate sub-30 fs pulses while maintaining high peak power for the MPM excitation.

In this project, I investigate the feasibility of applying a specially-designed chirped photonic crystal fiber (CPCF) for MPM imaging. The reason is that the CPCF has unique cell-size radial chirp in the cladding structure which can eliminate most pulse broadening effects in a broadband transmission window. The key features of the CPCF are characterized, such as spectra, mode profile, and dispersion parameter, etc. A fiber-delivered MPM system is developed by adding the fiber coupling to a multimodal microscope. A prism-based dispersion pre-compensation unit is optimized to compensate the dispersion from all the optical components in the CPCF-delivered system. After pre-compensation, the high fidelity propagation of femtosecond pulses through the CPCF is demonstrated by imaging various biological samples. Additionally, traditional hollow core fiber (HCF) is used as a comparison. The HCF consists of several identical reflective layers in the cladding. Compared with the CPCF, the change in the arrangement of holes leads to different guiding mechanism and different dispersion properties. I pre-compensate the laser pulses after the HCF propagation and MPM images for similar samples are acquired. Large

improvement in image contrast is observed in all samples for the system using the CPCF for light delivery compared with the system using the conventional HCF. The enhancement in second harmonic generation (SHG) is more significant than that in two photon excited fluorescence (TPEF).

Our study shows that CPCF can successfully deliver sub-30 fs pulses with significantly increased excitation efficiency of MPM for the broad-band laser. Theoretically, CPCF can also be beneficial for the delivery of femtosecond pulses with tunable wavelength. These properties are highly sought after in MPM endoscopy. With the fiber delivery of femtosecond pulses, MPM can be developed into a portable system for *in vivo* imaging.

Preface

A version of chapter 2 and partial chapter 4 has been published. [Jiali Yu], *Proc. SPIE* 8588, Multiphoton Microscopy in the Biomedical Science XIII, 85882R (2013); “A study on the application of chirped photonic crystal fiber in multiphoton microscopy”. I conducted all the experiments and wrote the manuscript.

Chapter 3 is based on the previous work conducted in the Biophotonics laboratory at UBC by Dr. Tang and Yifeng Zhou. I was responsible for building the fiber-delivery sub-system, comparing the performance of two types of specific fibers, optimizing the pre-compensation, and measuring the pulsewidth after the propagation through the fiber.

A revised version of chapter 5 is under preparation for publication. I take charge of all the experiments and manuscripts.

Table of Contents

Abstract	ii
Preface	iv
Table of Contents	v
List of Tables	viii
List of Figures.....	ix
List of Abbreviations.....	xii
Acknowledgements.....	xiii
Dedication.....	xiv
Chapter 1: Introduction.....	1
1.1 Brief background of MPM.....	1
1.2 Fiber-based MPM endoscopes	6
1.3 Motivation.....	8
1.4 Personal contribution and collaboration	9
Chapter 2: Characterization of chirped photonic crystal fibers	11
2.1 Optical fibers currently employed in MPM	11
2.1.1 Single-mode fibers (SMFs)	12
2.1.2 Double-clad fibers (DCFs)	12
2.1.3 Photonic crystal fibers (PCFs).....	13
2.2 Fibers adopted in this project	15
2.2.1 Conventional hollow core fibers.....	16
2.2.2 Chirped photonic crystal fibers (CPCFs)	17

2.3	Spectrum of the CPCF	19
2.4	Spatial mode profile of the CPCF	21
2.5	Loss of the CPCF.....	23
2.6	Numerical aperture and energy density of the CPCF	26
Chapter 3: System schematic.....		28
3.1	Layout for MPM imaging system.....	28
3.2	Dispersion pre-compensation unit	30
3.3	Setup for characterizing the propagation properties of fibers	31
Chapter 4: Characterization of the dispersion of CPCF and HCF		33
4.1	Dispersion	33
4.1.1	Prism-based dispersion compensation	36
4.1.2	Intensity autocorrelator as a measurement of pulse duration	40
4.2	Pulse broadening due to dispersion from various lenses	42
4.3	Characterization of the dispersion of CPCF.....	46
4.3.1	Assessment of GVD without pre-compensation	46
4.3.2	Pulwidth with different fiber length under dispersion pre-compensation	48
4.3.2.1	Autocorrelation trace of a CPCF with short length.....	49
4.3.2.2	Autocorrelation trace of a CPCF with longer length	50
4.4	Comparison with the dispersion characterization of HC-800-01	52
4.4.1	Assessment of GVD without pre-compensation	52
4.4.2	Autocorrelation with pre-compensation.....	53
Chapter 5: System image demonstration		56
5.1	Imaging biological samples based on fiber-delivered system.....	56

5.1.1	Imaging human skin based on fiber-delivered system.....	58
5.1.2	Imaging human tooth based on fiber-delivered system	62
5.1.3	Imaging fish cornea with system through light delivered by the CPCF and free space microscopy system	65
5.2	Quantitative comparison of image intensities obtained by the two types of fibers.....	68
5.2.1	Calibration by fluorescent beads images and fish scale.....	69
5.2.2	Comparison for dermis layer in human skin	74
Chapter 6: Conclusion		79
6.1	Conclusions	79
6.2	Future work	80
Bibliography		82

List of Tables

Table 1.1 Features of TPEF and SHG.....	6
Table 2.1 Specification of the HC-800-01	17
Table 2.2 Measurement of numerical aperture of the chirped fiber	26
Table 4.1 Pulsethickness of various lens combinations without and with pre-compensation	45
Table 5.1 The intensities of fluorescent beads and fish scale for two fiber-delivered systems and corresponding enhancement	74
Table 5.2 The intensities of human skin in five locations for two fiber-delivery configurations and the corresponding enhancement	78

List of Figures

Figure 1.1 Physical principle of MPM.	3
Figure 1.2 Multiphoton excitation characteristics of intrinsic fluorophores in 700-1000 nm range.	5
Figure 2.1 Schematic of a single mode fiber.	12
Figure 2.2 Schematic of a double-clad fiber.....	13
Figure 2.3 Scanning electronic micrographs of photonic crystal fibers.....	15
Figure 2.4(a) Optical micrograph of a commercial HCF (thorlabs HC-800-01); (b) the attenuation and dispersion curve of the HC-800-01.	17
Figure 2.5 Optical micrograph of a chirped photonic crystal fiber with 50 μm core.	19
Figure 2.6 Measurement of transmission window of CPCF..	20
Figure 2.7 Spectra of laser beam before and after propagating through a CPCF with 0.8 m length and a HC-800-1 with 0.4 m length.....	21
Figure 2.8 Far-field beam profiles at a CPCF end with 0.4 m length. (a)-(c) occur when slightly adjusting the fiber tip by three-dimensional stage.	22
Figure 2.9 Far-field beam profiles after a CPCF delivery with 1.2 m length.....	23
Figure 2.10 Layout for measuring the propagation loss of CPCF..	24
Figure 2.11 Measurement of bending loss for CPCF.....	25
Figure 3.1 Optical schematic of fiber-delivered system for MPM imaging demonstration.....	29
Figure 3.2 Layout of a double-folded prism pair as the dispersion pre-compensation unit.....	31
Figure 3.3 The configuration of measuring the fiber properties.....	32
Figure 4.1 Schematic of optical path of double-folded prism pair.	37

Figure 4.2 The geometry of a light ray traversing a prism.....	38
Figure 4.3 Principle of intensity autocorrelation.	42
Figure 4.4 Calculated GDD introduced by the prism pair.....	44
Figure 4.5 Intensity autocorrelation measurements for different cases without the dispersion compensation.	48
Figure 4.6 Intensity autocorrelation measurements of a 0.4 m CPCF and laser itself with optimal dispersion compensation.	50
Figure 4.7 Intensity autocorrelation measurements of the 1.2m CPCF at sample location with optimal dispersion compensation.....	52
Figure 4.8 Autocorrelation trace of the 0.4 m HCF at fiber tip without pre-compensation.....	53
Figure 4.9 Autocorrelation trace of the 0.1 m HCF at the fiber end under the pre-compensation.. ..	54
Figure 4.10 Autocorrelation trace of the 0.4 m HCF at sample location with pre-compensation.. ..	55
Figure 5.1 MPM images for Yew leaf based on two fiber-delivery systems.. ..	57
Figure 5.2 MPM images for rat-tail tendon based on two fiber-delivery systems.. ..	57
Figure 5.3 Anatomy of human skin.	59
Figure 5.4 MPM images of human skin when power delivered by 0.8 m CPCF on the sample is 5 mw; Integration time per pixel for all images is 10 μ s. The scale bar is 50 μ m.	60
Figure 5.5 MPM images of human skin when power delivered by the 0.4 m HC-800-01 on the sample is 5 mw; Integration time per pixel for all images is 30 μ s. The scale bar is 50 μ m.	61
Figure 5.6 Cross section of human tooth.....	63

Figure 5.7 MPM images of human tooth at different depths when power delivered by 0.8 m CPCF on the sample is 5 mw; Integration time per pixel for all images is 10 μ s..	64
Figure 5.8 MPM images of human tooth when power delivered by the 0.4 m HC-800-01 on the sample is 5 mw and integration time per pixel is 30 μ s.....	65
Figure 5.9 Anatomy of the cornea.	66
Figure 5.10 MPM images of fish cornea at different depths when power delivered by 0.8 m CPCF on the sample is 4 mw; Integration time per pixel for all images is 60 μ s..	67
Figure 5.11 MPM images of fish cornea at different depths when power on sample is 4 mW in the free-space microscopy system. Integration time per pixel for all images is 30 μ s..	68
Figure 5.12 TPEF images of fluorescent beads at same imaging condition for the 0.8 m CPCF and 0.4 m HC-800-01 by varied the illumination power on the sample. Pixel integration time for all images is 10 μ s.....	70
Figure 5.13 SHG images of fish scale at same imaging condition for the 0.8 m CPCF and 0.4 m HC-800-01.....	71
Figure 5.14 Images of the dermis layer of human skin using CPCF with 0.8 m length; Pixel dwell time is 10 μ s.....	76
Figure 5.15 cross-section images of the dermis layer of human skin using the HC-800-01 with 0.4 m length; Pixel dwell time is 30 μ s.....	77
Figure 6.1 Schematic of possible MPM endoscope.....	81

List of Abbreviations

MPM	Multiphoton microscopy
TPEF	Two-photon excitation fluorescence
SHG	Second harmonic generation
CPCF	Chirped photonic crystal fiber
HCF	Hollow core fiber
SMF	Single mode fiber
DCF	Double-clad fiber
PCF	Photonic crystal fiber
PBF	Photonic bandgap fiber
GVD	Group velocity dispersion
GDD	Group delay dispersion
SPM	Self-phase modulation
FWHM	Full width at half maximum
NA	Numerical aperture
PMT	Photomultiplier tube
NIR	Near infrared
NADH	Nicotinamide adenine dinucleotide
SC	Stratum corneum
SG	Stratum granulosum
SS	Stratum spinosum
SB	Stratum basale
DEJ	Dentin-enamel junction

Acknowledgements

I offer my enduring gratitude to my supervisor and collaborators, who have inspired me to continue my work in this field. Especially, I thank Dr. Shuo Tang for offering me the opportunity to work in her lab and providing me coherent answers to my endless questions.

I would also like to thank my fellow graduate students in the Biophotonic labs: Dr. Shau Poh Chong, Sandy Huang, Leon Zhou, Tom Lai, Leo Pan, Simon Shen, and M. J. Ju.

Special thanks are owed to my mother, who has supported me throughout my years of education, both morally and physically. To my husband Junqi Guo, I thank him for his understanding and support.

Jiali Yu

University of British Columbia

Dedication

To my parents, families and friends

Chapter 1: Introduction

In this chapter, the basic principles of multiphoton microscopy (MPM) and fiber-based multiphoton endoscopes are reviewed. Then, the challenges of current fiber-based multiphoton endoscopes are discussed and the novel chirped photonic crystal fibers (CPCF) are introduced. Finally, the outline of the whole thesis is previewed.

1.1 Brief background of MPM

The need for better visualization of cellular structures and tissue constituents inside various organs has triggered the advance of nonlinear optical microscopy. Particularly, MPM has become a widely used image modality for turbid tissues since three decades ago [1, 2]. For example, neuroscientists have used MPM to monitor the structure of neural compartments and to observe calcium dynamics networks in live animals [3-5]. Cancer researchers have used MPM for *in vivo* imaging of cells and extracellular matrix for studying metastasis and angiogenesis [6, 7]. Thus, MPM is an indispensable tool for high-resolution structural and functional imaging. In this work, we focus on two imaging contrast mechanisms in MPM which are two-photon excitation fluorescence (TPEF) [8] and second harmonic generation (SHG) [9].

MPM employs two or more photons to create excitation. In light-matter interactions, a material subjected to light generates a response called polarization. The induced polarization of material can be written as [10]

$$P = \chi^{(1)}E + \chi^{(2)}E^2 + \chi^{(3)}E^3 + \dots \quad (1.1)$$

where $\chi^{(1)}$ is the linear susceptibility, $\chi^{(n)}$ is the n th order nonlinear susceptibility (for $n>1$) and E is the electrical field of the incident light. Specifically, $\chi^{(1)}$ leads to normal linear interactions such as absorption and reflection of light, $\chi^{(2)}$ corresponds to SHG, and $\chi^{(3)}$ contributes to TPEF

and third-harmonic generation. Therefore, TPEF and SHG have different fundamental origins compared with single-photon microscopy such as confocal microscopy [11, 12].

In Fig 1.1, the energy diagrams of TPEF and SHG are described [13]. In TPEF, two photons with a lower energy are absorbed simultaneously to excite a molecule from the ground state to the excited state. In comparison, a single higher energy photon is absorbed to excite the molecule in single-photon excitation. The emission photon carries slightly less energy than the sum of the two excitation photons due to energy loss in the transitions. TPEF is an incoherent process where the emitted photons radiate independently and isotropically. Due to the extremely low probability of two-photon absorption, high flux of excitation photons is necessary to generate sufficient TPEF signals [14]. In the SHG process, rather than being absorbed, two excitation photons are simultaneously scattered and a SHG photon at exactly twice the energy of the excitation photon is created. Although real absorption is not a prerequisite, SHG is enhanced near an absorption resonance. Contrary to TPEF, SHG is a coherent process where the SHG photons experience constructive or destructive interference. Thus phase matching, which produces a highly forward-directed emission, is essential in SHG. Moreover, SHG requires non-centrosymmetric materials [10].

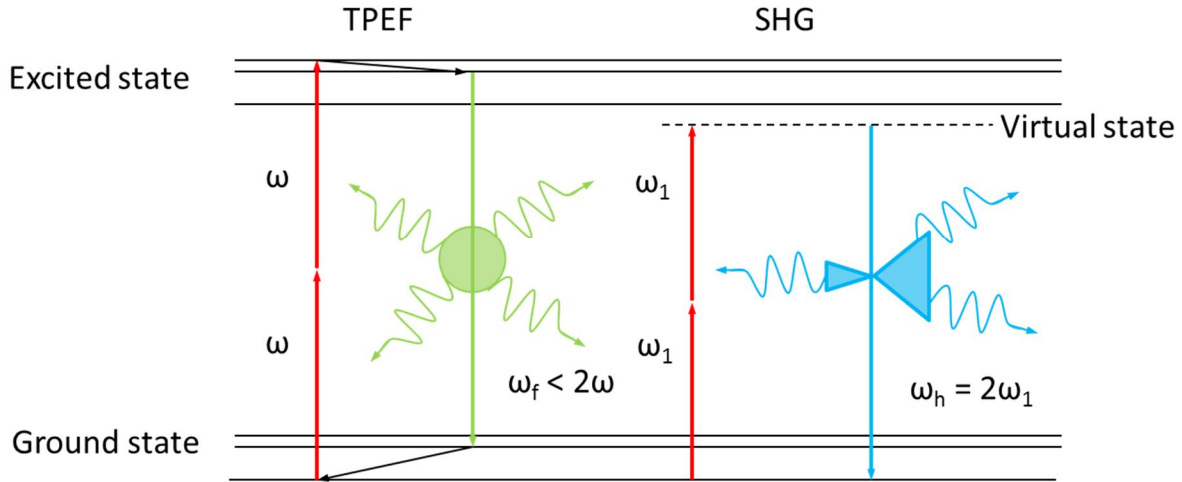


Figure 1.1 Physical principle of MPM [13].

Since the efficiency of two-photon absorption is extremely low, focusing the excitation light in the spatial and temporal domains is required to achieve high photon flux. In other words, the light should be focused by an objective lens with high numerical aperture (NA) and an ultrashort pulsed laser should be used to achieve high peak intensity. In TPEF, the number of photons absorbed through two-photon process per fluorophore per pulse is expressed by [15]

$$n_2 \approx \frac{P_{\text{ave}}^2 \delta}{\tau_p f_p^2} ((\text{NA})^2 / 2hc\lambda)^2 \quad (1.2)$$

where δ is the two-photon absorption cross-section, P_{ave} is the average laser intensity, τ_p is the pulsewidth, f_p is the pulse repetition rate, NA is the numerical aperture of objective lens, λ is the wavelength, h is Planck's constant, and c is the speed of light. In SHG, the emission strength is given by [10]

$$n_{\text{SHG}} \propto (\chi^{(2)})^2 P_{\text{ave}}^2 / (\tau_p f_p^2) \quad (1.3)$$

where P_{ave} , τ_p , and f_p have exact the same meaning as mentioned above. Therefore, both TPEF and SHG intensities scale quadratically with the excitation laser power but inversely with the pulsewidth of the laser.

TPEF and SHG prevail over single-photon microscopy (i.e., confocal microscopy) in several aspects. Firstly, both TPEF and SHG use low energy photons in the near-infrared (NIR) wavelength range for excitation. As a result, the penetration depth is increased due to less scattering in turbid tissue at NIR. Phototoxicity is also greatly reduced due to the lack of endogenous absorbers in tissue at NIR. Secondly, the intensity-squared dependence of TPEF and SHG enables localized excitation in the sub-femtoliter focal volume that offers high resolution in three dimensions. Typically, the lateral resolution is around 0.5 μm with a depth resolution of 1.5 μm . Thirdly, the inherent localized excitation at the focal volume reduces the photodamage in the light path and thus increases the viability of living tissues. Finally, the combination of TPEF and SHG provides the biochemical specificity. For instance, TPEF can be excited either from intrinsic tissue components (e.g., nicotinamide adenine dinucleotide (NADH), elastin, flavins and melanin) or from exogenous fluorophores [16]. NADH fluorescence can work as an indicator for cellular metabolic state because the coenzyme NADH is involved in redox reaction [17]. Substantial NADH can be found in the cellular cytoplasm in vertebrate bodies. Moreover, researchers addressed that neoplastic metabolism is associated with changes in the concentrations of NADH. Additionally, SHG can be detected in extracellular matrix such as collagen and muscle myosin in various tissues [18]. Collagen is abundant in the connective tissues and SHG imaging of collagen can distinguish the boundary between connective tissues and cells. Furthermore, it has been reported that the modification of collagen in tissues is associated with various pathological processes such as cancer [19, 20]. In sum, imaging intrinsic fluorophores is important for diagnosis and treatment of cancer.

In TPEF, the efficiency of emission signals strongly depends on the intrinsic two-photon absorption cross-section of the fluorophores, which is excitation wavelength dependent.

Understanding the relationship between the two-photon absorption cross-section and the excitation wavelength helps us to choose the optimal excitation wavelength for specific fluorophores in tissues. The excitation wavelength dependences for several intrinsic fluorophores commonly found in tissues are summarized in Fig. 1.2 [16].

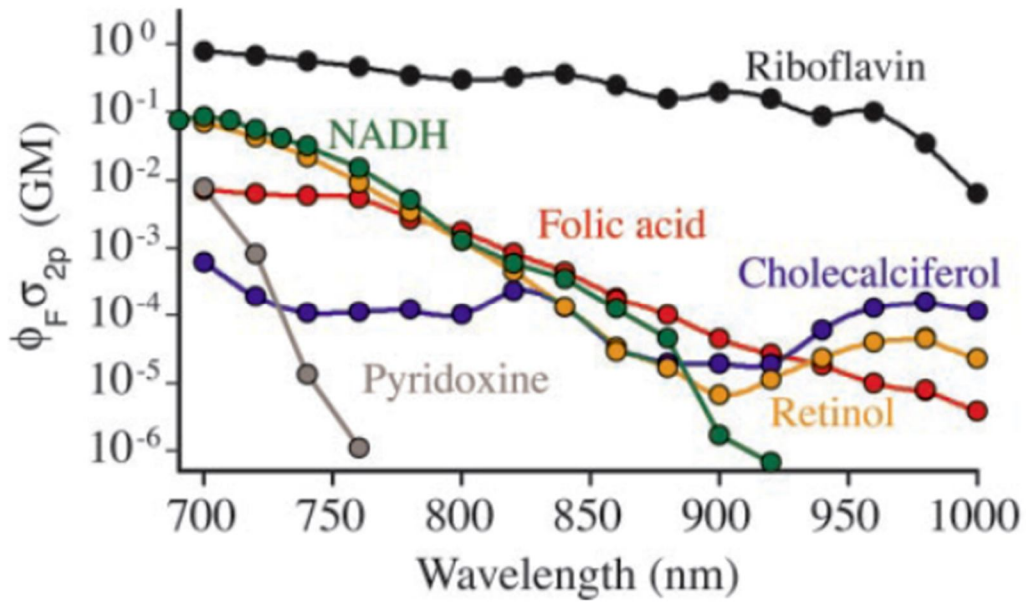


Figure 1.2 Multiphoton excitation characteristics of intrinsic fluorophores in 700-1000 nm range [16].

In conclusion, the characteristics of TPEF and SHG are summarized in Table 1.1.

Table 1.1 Features of TPEF and SHG

	TPEF	SHG
Corresponding Susceptibility	$\chi^{(3)}$	$\chi^{(2)}$
Year introduced to microscopy	Denk et al. in 1990 [8]	Hellwarth et al. in 1974 [21]
Endogenous origin	NADH, Elastin, Flavins, melanin, green fluorescence protein, etc.	Collagens, micro-tubules, and muscle myosin
Differences	<ul style="list-style-type: none"> • Incoherent process • Real absorption 	<ul style="list-style-type: none"> • Coherent process • Scattering without energy deposition • Occurs in non-centrosymmetric structures
Shared advantages	<ul style="list-style-type: none"> • Deep penetration depth • Inherent optical sectioning capability • Reduced photodamage and photobleaching 	
Disadvantages	<ul style="list-style-type: none"> • Low efficiency • High cost of lasers with ultrashort pulses 	

1.2 Fiber-based MPM endoscopes

Currently, most MPM instruments are based on bulky tabletop microscopes which greatly limit their clinical applications for *in vivo* imaging. Fiber-based multiphoton endoscopes permitting minimally invasive imaging of living organs can be applied in early cancer diagnosis and long-term disease monitoring [22, 23]. There is growing interest in developing fiber-based

multiphoton endoscopes for clinical applications due to their flexibility and miniaturization [24, 25].

Although numerous efforts have been made to develop MPM endoscopes, several key challenges remain. Firstly, the ultrashort pulses from excitation laser (20fs~200fs) need to be transmitted efficiently inside the fiber. Otherwise, the broadening of femtosecond pulses before reaching the sample dramatically reduces the strength of MPM signals. Secondly, the weak fluorescence signals need to be collected efficiently. Thirdly, miniaturized scanners with fast scanning rate are required for real-time imaging. Finally, the image quality from the probe-based micro-optics should be comparable to that acquired by tabletop microscopy.

In the following, a literature review on fiber-based MPM is conducted. A fiber-optics two-photon microscopy was reported by D. Bird and M. Gu using a single-mode fiber (SMF) [26]. After light delivery by a 1 m length SMF, the pulses with original duration of 80 fs were stretched to approximately 3 ps at the output of the fiber because of the group velocity dispersion (GVD) and strong nonlinear response [26]. W. Göbel et al. developed a miniaturized two-photon microscope based on a coherent fiber bundle with 30,000 individual cores. Although a pair of grating was employed as the dispersion pre-compensation unit, the two-photon excitation remained suboptimal due to the severe nonlinear broadening even at a low laser power (5 mW) [27]. A portable two-photon microendoscope was proposed by B. A. Flusberg et al. using a commercial photonic bandgap fiber which has zero GVD at around 795 nm. Pulses of 150 fs pulsewidth and 791 nm center wavelength suffered slight temporal broadening after transmitting in the 1.5 m length photonic bandgap fiber, perhaps due to higher-order dispersion [28]. Similarly, Göbel et al. demonstrated nearly distortion-free delivery of 170 fs pulses at the zero-GVD wavelength (812 nm). However, at above or below the zero-GVD wavelength, the output

pulse is significantly broadened, e.g. to 2 ps at 795 nm [29]. M. T. Myaing et al. achieved the fiber-optic scanning endoscope based on a double-clad fiber (DCF) for the delivery of illumination light and collection of fluorescence. They pointed out that the 1.37 m length double-clad fiber introduced $\sim 59,000 \text{ fs}^2$ dispersion under low excitation power ($< 10 \text{ mW}$) and it required a grating-based stretcher for dispersion compensation [30]. The application of double-clad photonic crystal fiber in the multiphoton field was investigated by several groups such as L. Fu et al. and S. Tang et al [31, 32]. Pulses with 170 fs duration were broadened to 2.5 ps after a double-clad photonic crystal fiber delivery with 2 m length [32].

From above, even though each type of fiber has its own advantages, none of them could directly deliver sub-30 fs pulses with high fidelity and high power. These fibers not only limit the maximum excitation intensity delivered in the fiber core due to nonlinear effects but also significantly broaden the femtosecond pulses to thus reduce the MPM emission signals. Even though most of the current systems use grating/prism stretchers to pre-compensate the large fiber dispersions, these fiber-based MPM systems can only deliver relatively long pulses of 80~200 fs duration.

1.3 Motivation

Although high power can greatly increase the TPEF/SHG signals, the laser power on the sample is limited by the photo-bleaching and photo-damage. Therefore, shortening the pulsewidth at the sample location is a better way to enhance the optical intensities in the time domain at a comparatively lower average power. However, a short pulse with high power suffers temporal and spectral distortion as it propagates through optical fibers, which lowers the

excitation efficiency of MPM. In consequence, how to efficiently deliver ultrashort pulses of broad-bandwidth laser through optical fibers in NIR is of great importance.

The goal for this thesis is to find a good candidate of fibers for fiber-based MPM endoscopes. The aim is to achieve sub-30 fs pulse at the sample location after propagating through fibers so that the MPM image intensities can be enhanced. A new CPCF reported by Skibina et al. [33] originally designed for femtosecond fiber lasers aroused our interest to study its performance in the MPM field. To implement the CPCF in multiphoton applications, accurate characterization of the CPCF should be required. In this thesis, we perform a thorough characterization of this novel fiber, including the pulse broadening, spatial modes, and nonlinear effects, etc. The CPCF is then implemented in a fiber-based MPM system and the imaging performance is evaluated and validated by imaging various biological samples. To demonstrate the advantage of the CPCF, the characteristics and imaging performance using a commercial photonic crystal fiber are also investigated and compared.

1.4 Personal contribution and collaboration

The chirped photonic crystal fibers are provided by our collaborator Dr. Julia S. Skibina and Dr. Günter Steinmeyer while the commercial photonic crystal fiber (HC-800-01) is obtained from Thorlabs (New Jersey, USA).

I build the fiber-delivery configurations and the corresponding calibration system for characterizing the fiber propagation properties. The prism-pair as the dispersion compensation are previously built by Dr. Shuo Tang. My contribution is to reduce the dispersion from fiber-delivery lenses, to assure good coupling into the fibers, to optimize prism-based pre-compensation unit, and to investigate the temporal pulsewidth of the fibers under various

conditions, to clarify the possible reasons of satellites in the autocorrelation trace of the CPCF, to estimate the GVD of coupling lenses and the fibers used.

The work of MPM imaging sub-system was already done by Dr. Shuo Tang and previous master's student Yifeng Zhou. I implemented the CPCF to the imaging sub-system by delivering the laser pulses through the fiber. I shared the MPM imaging system and the software in this project to demonstrate the feasibility of applying the CPCF in MPM. The image acquisition and data analysis are performed by myself. Co-registered or similar images are acquired by the system using laser pulses delivered by the CPCF and the HC-800-01. The quantitative comparison of the intensities in the representative images are performed and analyzed. I find the dramatic enhancement of the MPM image contrasts by using the CPCF delivery. I attribute it to the short pulsewidth and extended bandwidth of the excitation light on the sample.

Chapter 2: Characterization of chirped photonic crystal fibers

In this chapter, we review the fibers used in the MPM field. Then, one type of specific fiber called the CPCF is adopted for our experiments; a commercial hollow core fiber serves as a comparison. The features of the CPCF, including spectra, mode profile, NA, and energy density, are assessed and presented in chapter 2.

2.1 Optical fibers currently employed in MPM

Fibers are one of the major elements in the multiphoton endoscopy due to its flexibility and miniaturization. However, it is a big challenge to efficiently deliver ultrashort pulses through optical fibers in the NIR region because the femtosecond pulses inevitably suffer with severe temporal and spectral distortion due to dispersion and excessive power dependent nonlinear effects [e.g. self-phase modulation (SPM)] [34]. Dispersion includes the material dispersion and waveguide dispersion, which can be balanced by the dispersion compensation devices. However, the nonlinear SPM is hard to be compensated. Typically, SPM is proportional to the cube of the intensity and inversely proportional to the square of the fiber diameter. Therefore, increasing the fiber diameter could dramatically reduce the effect of SPM. Furthermore, the spectral bandwidth strongly affects the pulse broadening. For example, a pulse with 200fs duration is minimally affected while a pulse with 20fs is stretched to more than 10 times when propagating through the same material [35]. In the following, various kinds of fibers that are currently used in MPM are discussed to give a thorough understanding about the femtosecond pulse propagation through the fibers.

2.1.1 Single-mode fibers (SMFs)

In a SMF, a core has a higher refractive index than a cladding layer in order to meet the total internal reflection principle [Fig. 2.1]. Typically, such fibers have a core size between 5~8 μm with low NA. On the one hand, such a small core causes excessive power-dependent nonlinear phenomena. For instance, for 100 fs pulses at center wavelength 800 nm with an average power of 400 mW, nonlinearity dominates the propagation and quickly distorts the spectrum even after 1.2 cm fiber delivery [36]. On the other hand, the material dispersion of silica fibers naturally cancels with the waveguide dispersion near 1300 nm-wavelength. This zero-GVD wavelength (1300 nm) is far away from the operating wavelength (800 nm) in MPM. Thus, a large amount of GVD in a SMF produces severe pulse distortions. In sum, the nonlinear effects restrict the maximum illumination power to 10 mW and the GVD broadens the pulse duration after SMF delivery. Both phenomena reduce the efficiency of MPM signals.

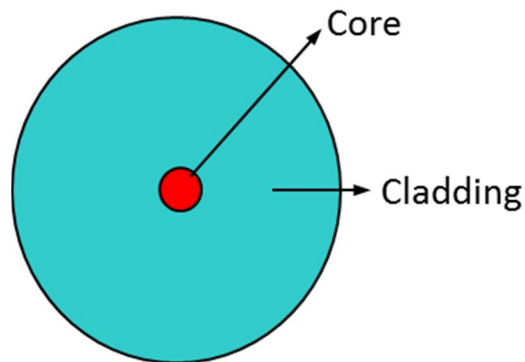


Figure 2.1 Schematic of a single mode fiber.

2.1.2 Double-clad fibers (DCFs)

As shown in Fig. 2.2, a DCF has a center single-mode core surrounded by an inner cladding which acts as a multimode fiber. The refractive index reduces from the core, inner

cladding, to an outer cladding. Femtosecond pulses can be delivered through the single-mode core and MPM signals can be collected by the core and the inner cladding. The collected signals are enhanced due to large NA of the inner cladding. Therefore, the advantage of a DCF lies in the fact that delivery of illumination light and collection of fluorescence can be achieved simultaneously. The limitation, similar to the SMF, is pulse broadening and nonlinearity (i.e., SPM).

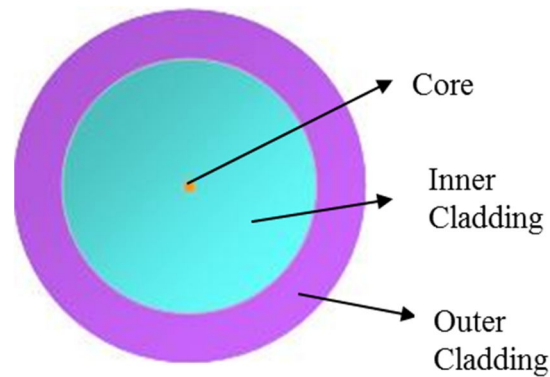


Figure 2.2 Schematic of a double-clad fiber.

2.1.3 Photonic crystal fibers (PCFs)

A recently developed microstructured fiber known as PCF can overcome the limitations of a conventional solid fiber and revolutionize the field of optical fiber [37, 38]. PCFs are characterized by a periodic array of the wavelength-scale air holes that extend over the entire length of the fiber. Although the appearance of PCFs vary a lot, PCFs usually can be divided into three categories based on the guiding mechanisms [39]. The first type is called hole-assisted fiber [Fig. 2.3(a)] [40]. They still follow the revised total internal reflection principle since a solid core has a higher index than a surrounding cladding in them. The second type is called photonic bandgap fiber (PBF) [Fig. 2.3(b)] [40]. The carefully designed cladding creates a photonic

bandgap that can confine light even in an air core. In the full bandgap guiding, the center core as a lattice defect violates the periodicity and thus forms the strict bandgap analogous to an electronic bandgap [Fig. 2.3(c)]. Owing to the boundary condition, spectral components in the photonic bandgap can be completely reflected by the cladding and can only propagate through the air core. Therefore, the strict photonic bandgap can only be formed in a relatively narrow spectral range. The third type is called quasi-guiding photonic crystal fiber [Fig. 2.3(d)] [39]. Compared with PBF, the direct bandgap is missing in the density of optical states diagram for quasi-guiding fiber [Fig. 2.3(e)]. So the core mode propagating in the air core can leak into air-silica holes in the cladding layer, leading to increased loss. The quasi-guiding fiber could allow a 20-times broader bandwidth than full bandgap guiding fiber. And the dispersion can be manipulated by adjusting the size of the holes and arrangement of holes in the cladding. No matter what kind of guiding mechanisms, the photonic crystal fibers with the hollow core are generally defined as the hollow core fibers (HCFs). Interestingly, HCF can circumvent nonlinear limits imposed by available materials and reduce the material dispersion as well as managing the waveguide dispersion [41].

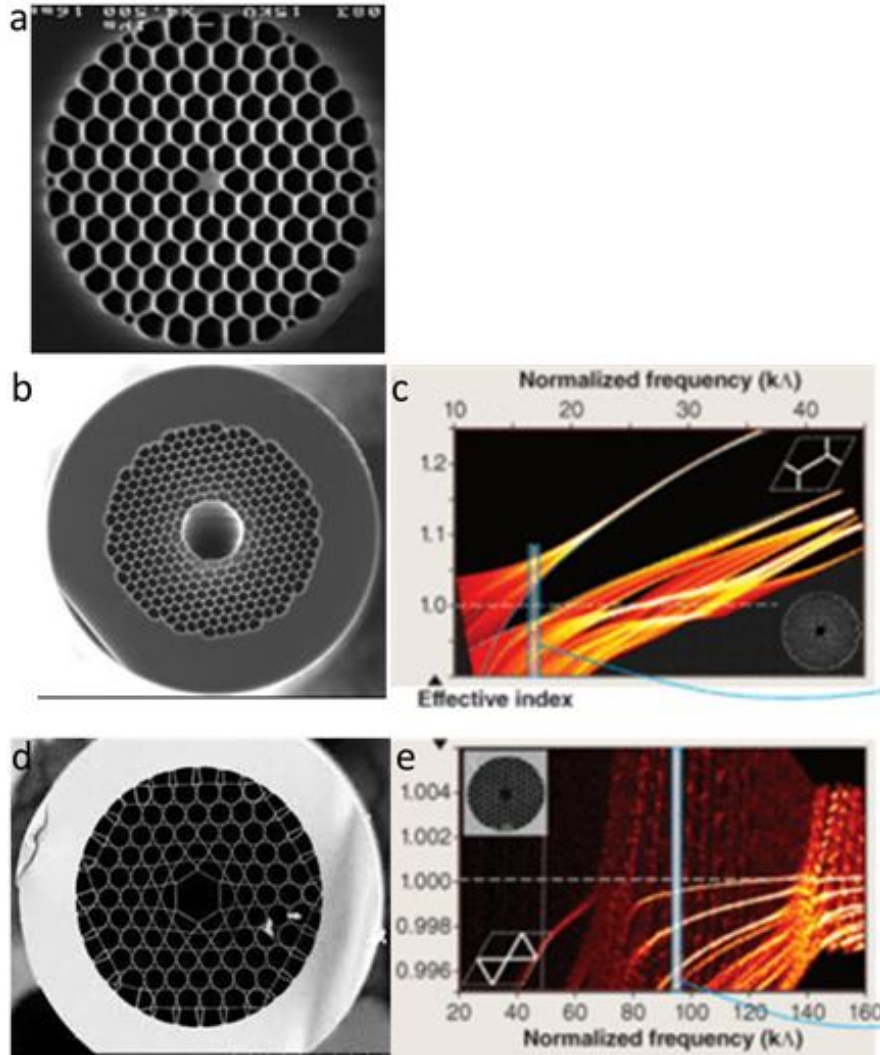


Figure 2.3 Scanning electronic micrographs of photonic crystal fibers. (a) a hole assisted photonic crystal fiber based on the revised total reflection [40]. (b) photonic bandgap fiber based on strict bandgap guiding [40]; (c) illustration of the density of optical states in full bandgap guiding [39]; (d) photonic crystal fiber based on quasi-guiding [42]; (e) illustration of the density of optical states in quasi-guiding [39].

2.2 Fibers adopted in this project

From the above description, we infer that the hollow core photonic crystal fiber is suitable for the dispersion management of ultrashort pulses. In the following, we introduce two different HCFs used in this project.

2.2.1 Conventional hollow core fibers

The traditional HCF comprises a hollow core and several layers with identical air-hole cells as a cladding. Such a structure with strict bandgap leads to strong resonances, similar to a Bragg reflector. Although traditional HCFs render relatively low dispersion and nonlinear effects compared to SMFs and DCFs, the total dispersion of conventional HCFs typically changes from normal to anomalous within a relatively narrow spectral band [43]. Consequently, zero GVD is practically achieved only at a single wavelength in the transmission band of HCFs. Furthermore, considerable higher-order dispersion of HCFs may even surpass that of a SMF at the same wavelength [43]. Several groups have investigated the properties of HCF-based MPM systems. For instance, Tai et al. showed that 200 fs pulse at 780 nm is stretched up to 4.88 ps after 1 m long HCF beyond the zero-GVD point (755 nm) [44]. Hence, the difficult-to-compensate higher-order dispersion strongly restricts the applications of HCFs to pulses with duration larger than 100 fs.

In Fig. 2.4(a), a commercial HCF (Thorlabs HC-800-01) employed in our experiments is shown. The core diameter of HC-800-01 is 9.5 μm and transmission band is about 70 nm at 0.35 dB/m loss due to the mature technology. The dispersion curve of HC-800-01 shown in Fig. 2.4(b) indicates a GVD at 790 nm of approximately $D = -150 \text{ ps/nm} \cdot \text{km}$, corresponding to $k_2 = 45,000 \text{ fs}^2/\text{m}$ [45]. Although an exact number of the third-order dispersion parameter (k_3) is not specified, a large slope of $dD/d\lambda$ is evident in the dispersion curve. The main parameters of the HC-800-01 are summarized in Table 2.1. Details about the different dispersion parameters will be explained in more details in Chapter 4.

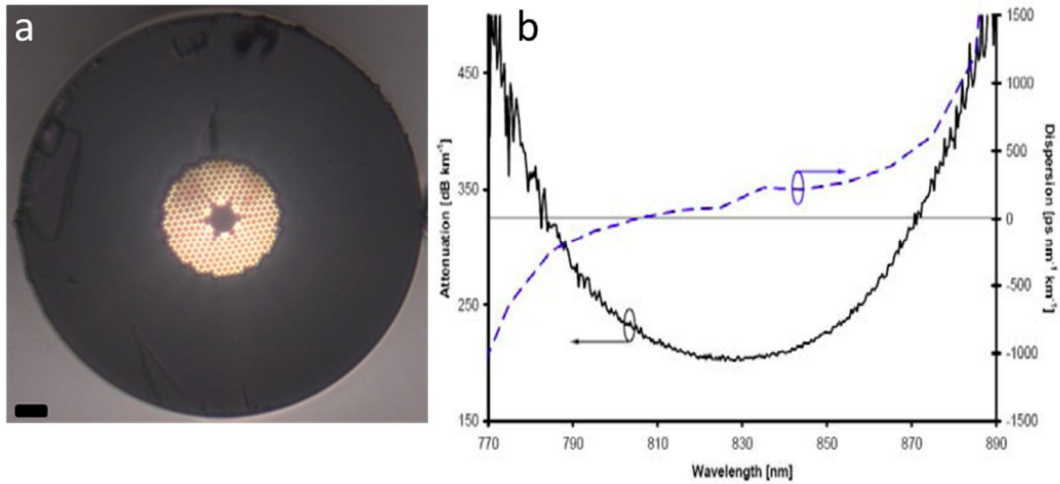


Figure 2.4(a) Optical micrograph of a commercial HCF (thorlabs HC-800-01); Scale bar is 10 μm . (b) the attenuation and dispersion curve of the HC-800-01 [45].

Table 2.1 Specification of the HC-800-01 (sourced from the datasheet [45])

Properties	
Core diameter	$9.5 \pm 1 \mu\text{m}$
Diameter of holey region	$40 \mu\text{m}$
Zero-GVD wavelength	812 nm
Attenuation (790~870 nm)	$< 0.35 \text{ dB/m}$
NA	0.28

2.2.2 Chirped photonic crystal fibers (CPCFs)

The term CPCF describes a special type of HCF with a cladding where the geometrical dimension changes in radial direction [33]. Specifically, the CPCF we used in the experiments consists of a five-layered cladding with increasing hole-sizes from inner to outer layer. This radial chirp in cell-size is actively introduced, analogous to the principle of chirped mirrors.

Therefore, light of different wavelengths is reflected at different layers of the chirped cladding in the CPCF, which introduces group delay variations with wavelength and tailors the dispersion profile effectively. As explained in greater details in [46], the introduction of a chirp into the structure in combination with unavoidable dimensional variations of the fiber structure actually serves to wash out the detrimental dispersive resonances. This unique fiber design therefore enables almost total elimination of dispersion. Distinct from commercial HCF, the CPCF is based on the quasi-guiding that results in moderately increased guiding loss.

Figure 2.5 shows a cross-section of a CPCF with 50 μm -core size taken by a 20X objective lens. Remarkably, the size of unit cells keeps increasing in a certain ratio (0.85:1) between any two adjacent layers from the inner side to the outer side. From the previous publication [33], we know that its k_2 appears on the order of a few fs^2/m to $100 \text{ fs}^2/\text{m}$ over the whole transmission band (720 nm to 820 nm). Moreover, the 50 μm core size of the CPCF is sufficiently large to relax the power limitation for nonlinear effects. All these advantages come with the cost of increased propagation attenuation, which will be discussed in Section 2.5.

It should be mentioned that CPCF is made from a soft optical glass C89-1 that is suitable for drawing such complicated structure. Therefore, a CPCF is more fragile than a traditional HCF and cleaving a CPCF becomes a challenge. The standard fiber cleaver for SMF or multimode fiber is not suitable for the CPCF. To cleave a CPCF, we use a ceramic cutter since ceramics is harder than glass. Firstly, we tape one end of the CPCF to the edge of a clean region on the optical table. Secondly, the ceramic cutter is applied perpendicularly to scribe the fiber to make a slight incision while the other end of the fiber is pulled straight back until the fiber cleaves. The cleaving quality is examined under an optical microscopy. Unfortunately, the angle of the end-surface is hard to control precisely due to manual cleave, lowering the coupling

efficiency. Moreover, the cleaved CPCF end-surface is forbidden to be cleaned by liquid solvents since moisture or liquid can enter into the holey channels to cause the deterioration of the guiding performance. After the cleaving, fiber tip should be carefully untouched to avoid damage or dirt that can cause poor laser coupling or increased dispersion.

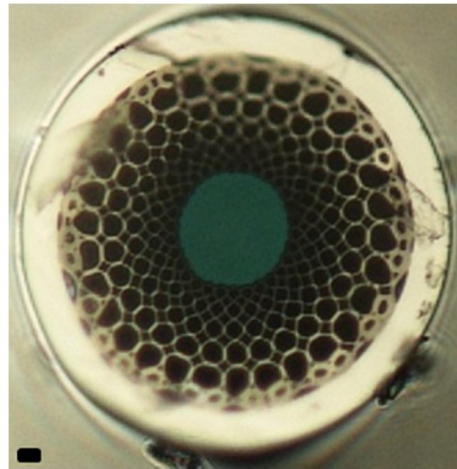


Figure 2.5 Optical micrograph of a chirped photonic crystal fiber with 50 μm core; Scale bar is 10 μm .

2.3 Spectrum of the CPCF

When fiber is employed to deliver the ultrashort pulse or to collect MPM signals, the transmission window should be measured since excitation light is around 800 nm and MPM signals are from 375 nm to 650 nm.

As shown in Fig. 2.6(a), the spectrum of white light source and corresponding spectrum after CPCF transmission are measured separately. In frequency domain, transmission window of the CPCF is acquired by dividing two spectrums. Figure 2.6(b) clearly shows two bands, one is around 510 nm and another is around 800 nm. The white light source we used lacks the spectral components in NIR. Therefore, the full band around 800 nm cannot be achieved. Due to

uncontinuous transmission band of CPCF, CPCF only can be used as the delivery fiber for the MPM endoscope.

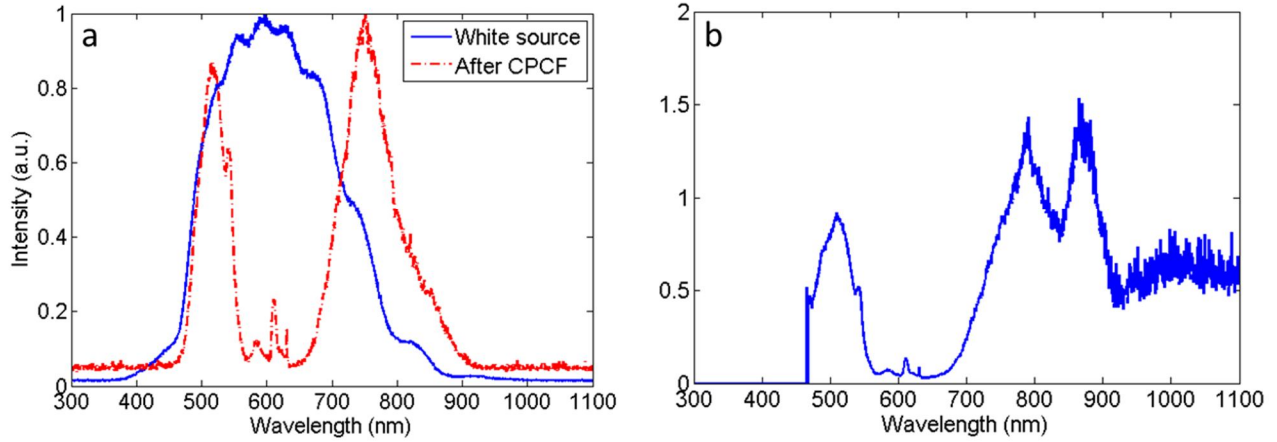


Figure 2.6 Measurement of transmission window of CPCF. (a) White-light spectrum of source and after CPCF delivery. (b) Transmission window of CPCF.

When using a fiber to deliver femtosecond pulses, the original spectrum of the pulses can be altered by the fiber due to limited propagation bandwidth. As described in Section 1.1, the two-photon absorption cross-section of the fluorophores depends on the excitation wavelength. TPEF intensities scale with the two-photon absorption cross-section. So TPEF intensities also have wavelength dependence. Therefore, the proper transmission window of the fiber should be taken into account for increasing TPEF intensities.

Figure 2.7 shows the spectrum of the laser output as well as that after the delivery through a CPCF and a HC-800-01. The band of our Ti:Sapphire laser (Femtolasers, Fusion PRO 400) is from 740 nm to 831 nm, corresponding to a full width at half maximum (FWHM) of 91 nm. After transmitting through fibers, the red line clearly shows that the bandwidth after the CPCF is slightly reduced to 85 nm while the green curve indicates that bandwidth after the HC-800-01 is

shortened to 64 nm. The small oscillations on the spectra are possibly due to the reflection from the fiber end-tip and coupling lenses. For the HC-800-01, the wavelengths below 730 nm are forbidden to propagate due to strict bandgap. As opposite to the HC-800-01, the CPCF does not have an obvious cut-off wavelength in the range of 700-900 nm, which enables a wider bandwidth. Furthermore, CPCF has an extended bandwidth especially in the short wavelength range compared to HCF. This feature can increase the two-photon fluorescence signals for some important endogenous fluorophores (e.g. NADH, elastin, etc.) which have two-photon absorption peaks between 700 to 730 nm.

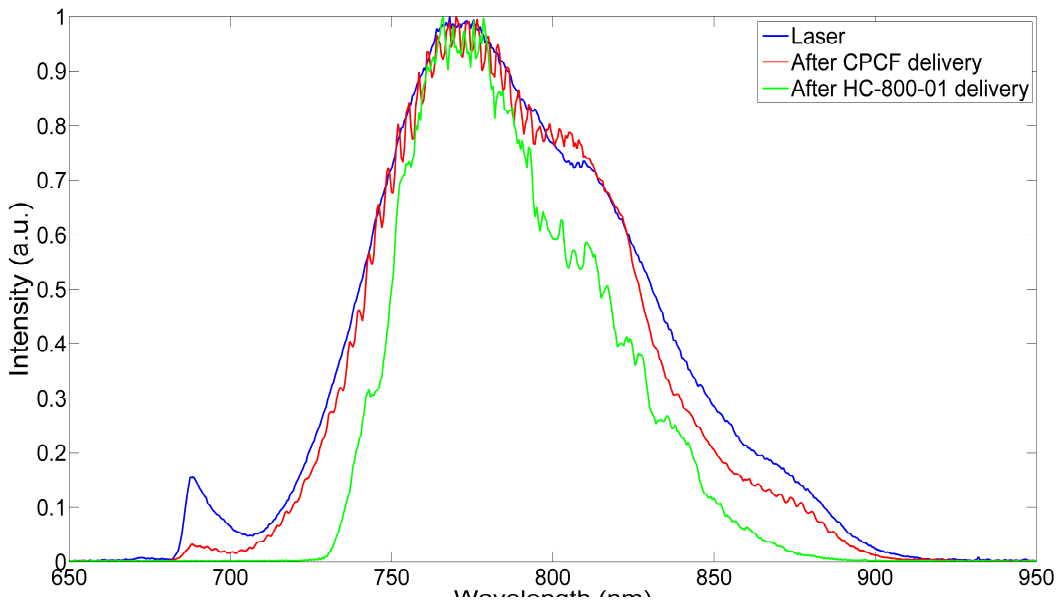


Figure 2.7 Spectra of laser beam before and after propagating through a CPCF with 0.8 m length and a HC-800-1 with 0.4 m length.

2.4 Spatial mode profile of the CPCF

As we mentioned before, a CPCF is based on quasi-guiding which means that none of the spatial modes is really lossless. However, the fundamental mode has less loss than higher-order

spatial modes. Meanwhile, single mode transmission after the fiber should be maintained because extremely large mode dispersion can arise between spatial modes, which could dramatically stretch the pulse and lower the MPM efficiency.

In order to study the output modes, the far-field beam profiles after light propagating through a 0.4m-CPCF are recorded by a CCD camera (Matrix vision, MvBlueFox). As shown in Fig. 2.8(a), the output seems like a fundamental mode while higher-order modes obviously appear in Figs. 2.8(b)-(c). The different mode profiles are obtained when changing the alignment of the CPCF coupling.

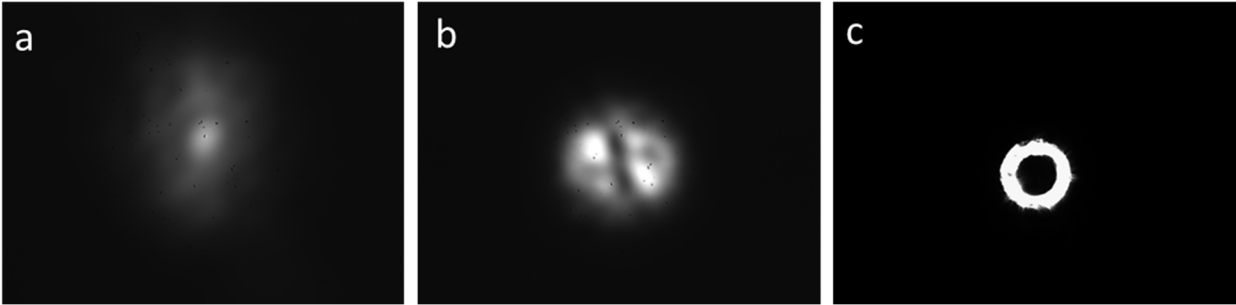


Figure 2.8 Far-field beam profiles at a CPCF end with 0.4 m length. (a)-(c) occur when slightly adjusting the fiber tip by three-dimensional stage.

In contrast, the fiber output mode after a 1.2 m CPCF propagation is measured by the CCD camera and displayed in Fig. 2.9(a). Figs. 2.9(b) and 2.9(c) show the Gaussian fit to the original data in horizontal and vertical directions. Clearly, the output mode of the light is close to Gaussian shape, which proves that the mode is primarily fundamental. This is because the higher spatial modes have been attenuated after 1.2m CPCF transmission due to their much higher loss in the quasi-guiding CPCF. Therefore, the CPCF requires a sufficient transmission length to suppress the higher spatial modes in order to obtain clean single mode propagation. From our

experiments, we found that the length of the CPCF should be longer than 0.8 m in order to maintain single mode delivery.

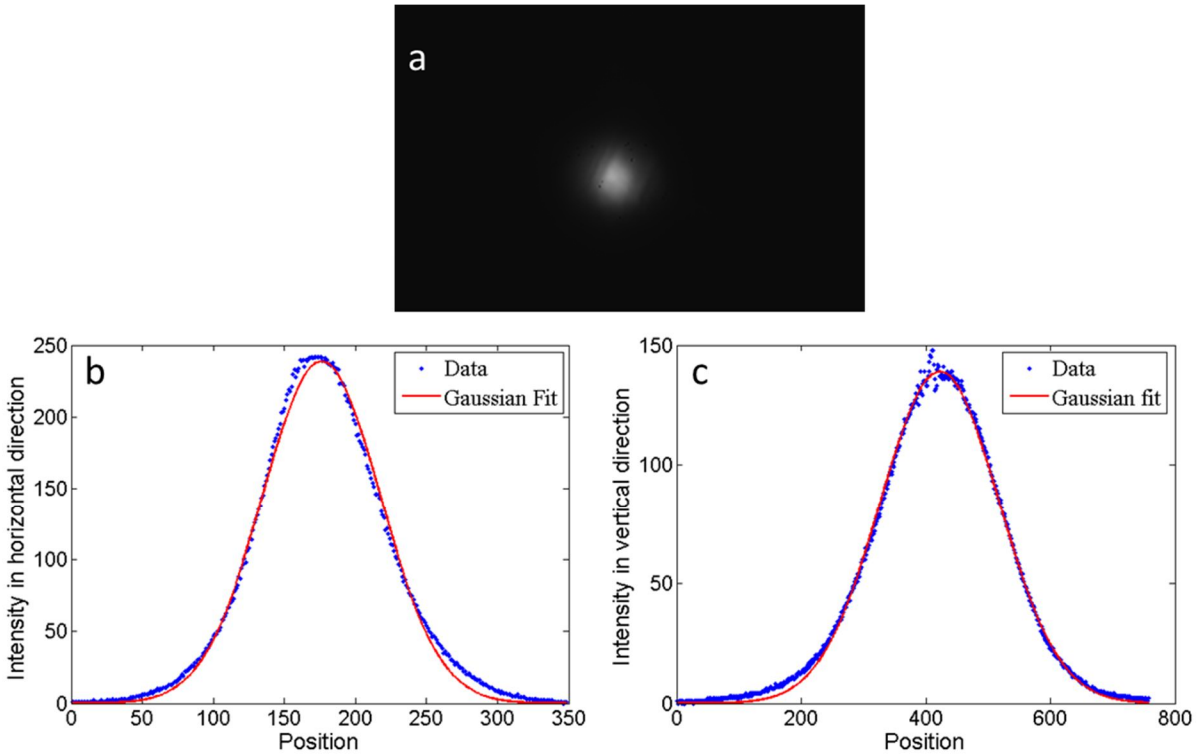


Figure 2.9 Far-field beam profiles after a CPCF delivery with 1.2 m length. (a) CCD image of fiber output mode; (b) Intensity distribute of the mode in the horizontal direction and corresponding Gaussian fit; (c) Intensity distribute of the mode in the vertical direction and corresponding Gaussian fit.

2.5 Loss of the CPCF

The propagation loss of the CPCF is vital to determine how much power can be delivered at the output end. More power after the CPCF transmission is welcomed for MPM application. Moreover, a large bending loss is observed if the CPCF is bent too tightly. This physical bending deforms the fiber cross-section that easily breaks the confinement of the core-mode. When the critical bending radius is reached, bending loss increases dramatically. However, a certain degree

of bending is essential in the application of MPM fiber-based endoscope. Therefore, the critical bending radius should be investigated.

In order to measure the propagation loss of CPCF, two pieces of CPCFs with different lengths are chosen [Fig. 2.10]. The CPCFs are placed straight to avoid bending loss.

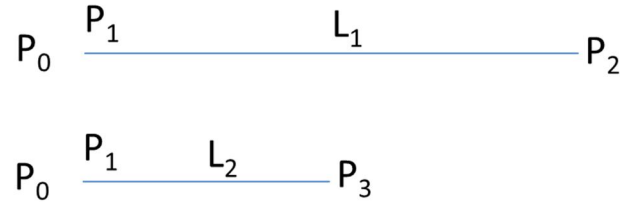


Figure 2.10 Layout for measuring the propagation loss of CPCF. P_0 is the laser input power, P_1 is fiber input power after coupling, P_2 and P_3 are fiber output power after each delivery, respectively. L_1 and L_2 are the lengths of each fiber.

Assuming the coupling efficiency maintains the same for each fiber, the propagation loss (α_p) and coupling efficiency (η) can be calculated by the following equations.

$$\alpha_p = -\frac{10}{L_1 - L_2} * \log_{10} \frac{P_2}{P_3} \quad (2.1)$$

$$\eta = \frac{P_2}{P_0} * 10^{\frac{\alpha_p L_1}{10}} \quad (2.2)$$

Using equation (2.1), the propagation loss of CPCF is estimated as 5.1 ± 2 dB/m. The coupling efficiency for CPCF with 50 μm core size is around 98.5%.

The bending loss is characterized in order to find critical radius. By using 1.35 m CPCF, we bend fiber in various radii and measure the corresponding power at output tip. The CPCF is returned back to straight layout and output power for straight CPCF is recorded. Afterwards, we obtain ratios between output power of bending CPCF and straight CPCF. The bending loss can be expressed by

$$P_{bent} = P_{straight} * \exp(-\alpha_b * \text{length of bend}) \quad (2.3)$$

$$\alpha_b(\text{dB/m}) = 4.34 * \alpha_b(1/\text{m}) \quad (2.4)$$

The estimated result of bending loss is plotted in Fig. 2.11. Once bending radius is around 5 cm, bending loss reaches over 6 dB/m and output power drops dramatically after CPCF delivery. Therefore, the critical radius is close to 6 cm for CPCF. The suggested bending radius should be larger than 15 cm in MPM endoscope application to avoid large extra loss. In contrast, common SMF (for instance, SM750 fibercore) only has negligible bending loss ~0.09 dB/km when bend radius reaches 2 cm. It should be stressed that bend loss of SMF is influenced by the NA, cut-off wavelength and operational wavelength. Although different SMFs induce different bend loss, bend loss is typically tiny when radius is bigger than 2 cm. For the commercial HCF (HC-800-01), the bend loss is also pretty small (< 0.15 dB/m) when bend radius is ~ 1 cm. Thus, the bending loss of CPCF is much larger due to loose confinement of core mode.

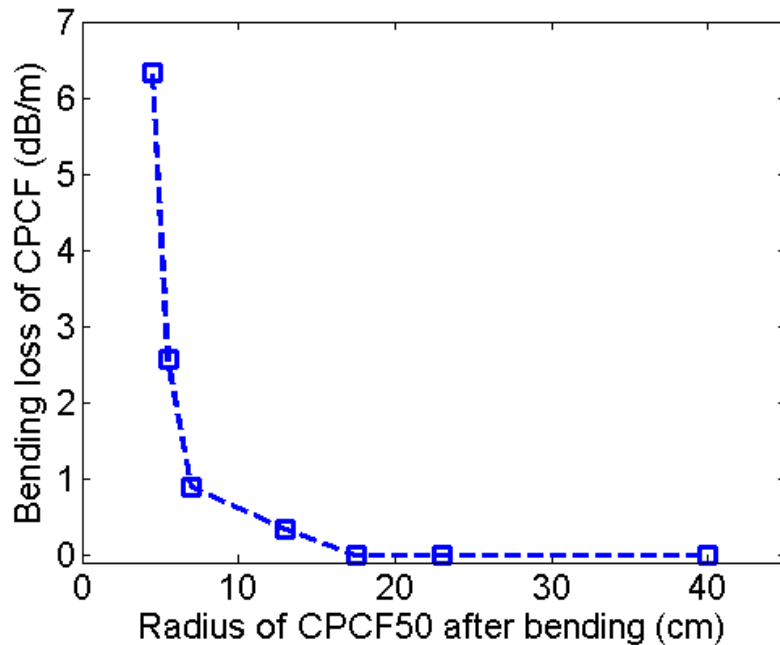


Figure 2.11 Measurement of bending loss for CPCF.

2.6 Numerical aperture and energy density of the CPCF

The NA of the CPCF is measured in order to optimize the fiber coupling efficiency. The spot sizes at certain distances from the fiber tip are recorded and measured manually. The measurements are repeated for the same piece of CPCF at three distances. Moreover, another piece of CPCF is also measured to consider any possible variation between different spools of the fiber. Table 2.2 shows the summarized results. The average NA of the CPCF is found to be around 0.027. Since NA of the CPCF is so low, the lens for fiber coupling should match with it.

Table 2.2 Measurement of numerical aperture of the chirped fiber

Distance from output fiber tip (mm)	Spot size (mm)	Estimated NA (average \pm standard deviation)
25	1.25 \pm 0.25	0.025 \pm 0.004
50	2.75 \pm 0.25	0.027 \pm 0.002
100	5.5 \pm 0.5	0.028 \pm 0.004
Average of NA		0.027 \pm 0.003

The laser power is crucial for the multiphoton imaging since more power produces more fluorescent signals from a sample. However, too much power in the fiber could damage the periodic structure and thus reduce the guiding efficiency. Furthermore, high power inside the fiber core could produce nonlinear effects that distort ultrashort pulses in temporal and spectral domains. Consequently, we examine the energy density inside the CPCF in the following.

$$Pulse\ energy = \frac{average\ power}{pulse\ repetition\ rate} = \frac{380mw}{80MHz} = 4.75\ nJ \quad (2.5)$$

$$Peak\ power = 0.94 * \frac{E_{pulse\ energy}}{\tau_{pulse\ duration}} = 0.94 * \frac{4.75\ nJ}{10\ fs} = 446.5\ KW \quad (2.6)$$

where 0.94 is a constant factor for Gaussian-shaped pulse.

$$Energy\ density_{CPCF} = \frac{Peak\ power}{\pi r^2} = 2.27 * 10^{10}\ W/cm^2 \quad (2.7)$$

$$Energy\ density_{HC-800-01} = \frac{Peak\ power}{\pi r^2} = 6.3 * 10^{11}\ W/cm^2 \quad (2.8)$$

where r is the radius of the mode field of fibers.

From the laser, the maximum average power is around 380 mw and the corresponding energy density on the CPCF is $2.27 * 10^{10}\ W/cm^2$. No obvious degradation on the cladding layer is observed at this power level when viewed under an optical microscope. In fact, the calculated energy density for the 50 μ m-core-size CPCF is far less than that of the traditional HCF. Thus, power-dependent SPM is significantly reduced in the CPCF.

Chapter 3: System schematic

We outline the basic characteristics of the novel CPCF in chapter 2. This chapter will introduce the fiber system setup in order to apply the fiber into MPM imaging, including optical schematic for MPM imaging with fiber delivered illumination, dispersion pre-compensation unit, and layout for testing the propagation properties of the fibers.

3.1 Layout for MPM imaging system

The experimental setup for investigating MPM imaging performance using the CPCF is shown in Fig. 3.1. Light generated from a Ti:Sapphire laser (Femtolasers, Fusion PRO 400) first passes through a dispersion pre-compensation unit. The center wavelength of the laser is around 800nm with a spectral bandwidth of 120nm. The pulse width is ~10 fs and the repetition rate is 80Mz. In some experiments, the pre-compensation unit is bypassed in order to measure the pulse broadening without dispersion compensation. A continuously variable neutral density filter enables the control of the laser power entering the fiber. After attenuation, the beam is coupled into a piece of the CPCF or the commercial HC-800-01. A pair of objective lenses (Olympus, Plan N 4X NA=0.1 and MPlanFL 10X NA=0.3) is used as the coupling and the collimation lens. In order to reduce the dispersion introduced by the two objective lenses, a spherical lens (Edmund NT69-476) and an aspherical lens (Newport 5X) are also tested as alternatives. The attenuator is adjusted to ensure identical output power level after light is delivered by the CPCF or the HCF. The beam after passing through the fiber enters an imaging sub-system denoted by a dashed box to examine the MPM imaging capability.

The imaging sub-system was designed and built previously for the multi-modality optical microscopy. Here, we share the same scanners and photo-detectors for the image acquisition in

the fiber-delivered configuration. As shown in the dashed box in Fig. 3.1, the beam is raster scanned by two galvanometer mirrors (Cambridge Technology, 6215H), expanded by two lenses, and eventually focused onto the sample by a 40X objective lens (Olympus, LUMPLANFL N) of 0.8 NA. The objective lens is mounted on a depth scanner (Piezosystem Jena, nanoMIPOS 400). The TPEF and SHG signals are collected in the backward direction by the same objective lens. The received signals are separated from the excitation light by passing through a short-pass dichroic mirror (Semrock, FF670-SDi01). TPEF and SHG signals are further separated from each other by a second dichroic mirror (Chroma, 450DCXRU) and then are respectively detected by two photomultiplier tubes (PMT) (Hamamatsu, H6780 and H5783P).

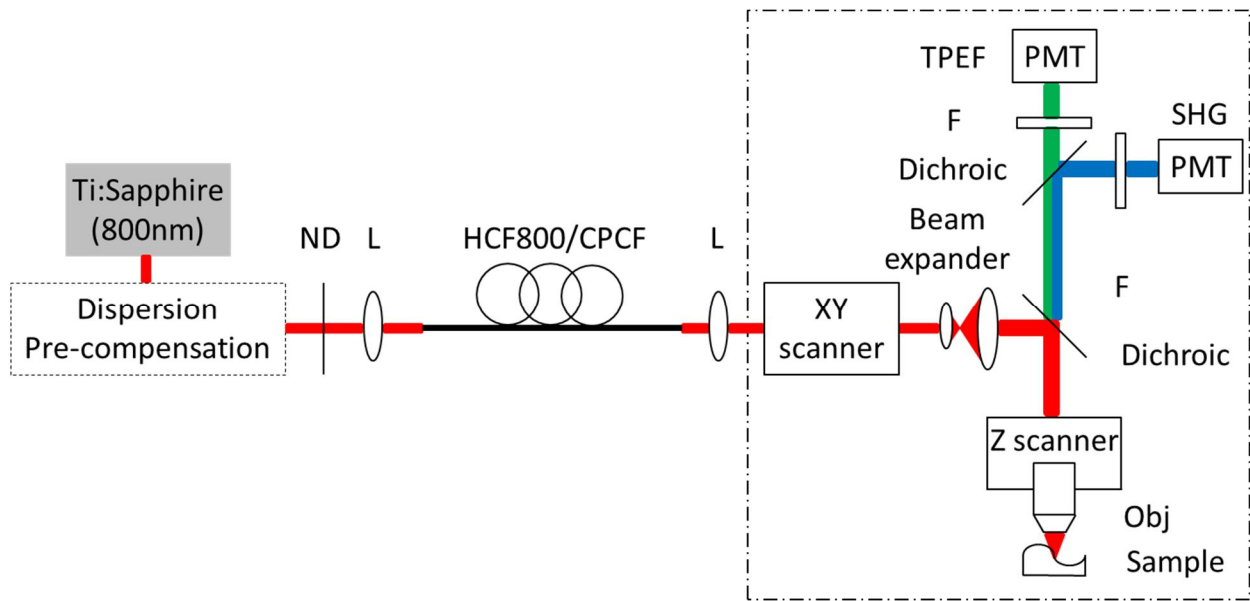


Figure 3.1 Optical schematic of fiber-delivered system for MPM imaging demonstration.

A data acquisition board (National instruments, PCIe-6363) is a core component for scanner control and image acquisition. A C++ program controls the data acquisition board to generate three analog outputs to separately drive the XY galvo scanners and the piezo scanner in

Z direction. Moreover, TPEF and SHG signals from each scanning point on the specimen are collected by each PMT, and input onto the data acquisition board. Thus, a stack of *en-face* MPM images based on fiber-delivered illumination can be obtained.

3.2 Dispersion pre-compensation unit

As shown in Fig. 3.1, the optical components except the fiber all introduce normal dispersion in the NIR region. Especially, objective lenses with high NA are compound lenses, which can introduce a large amount of dispersion and thus severely broaden the pulses. As a result, the dispersion from the objective lenses and other optical elements should be measured separately and compensated in order to verify the fiber performance. Therefore, anomalous dispersion is introduced by the pre-compensation unit to balance the normal dispersion from all the lenses used. Dispersion management can be achieved by using prism pairs, grating pairs or chirped mirrors [47, 48]. The principle is based on introducing a longer path-length for the wavelength component which travels faster. Chirped mirrors usually only compensate for small amount of dispersion and may be not sufficient to fully compensate for our fiber system [49]. Grating pairs can provide a large amount of anomalous GVD but add strong higher-order dispersion. The higher-order dispersion restricts the minimum pulsewidth that can be achieved after compression [50, 51]. For prism-based arrangement, altering the distance between the two prisms varies the amount of anomalous dispersion introduced from the prism pair, which simplifies the alignment when switching objectives in the microscope [52, 53]. Therefore, prism-based pre-compensation could be a good candidate for our application.

As shown in Fig. 3.2, the double-folded prism pair as a pre-compensation unit was previously accomplished by Dr. Tang and I use it for the fiber dispersion-compression. The

incident laser beam hits the apex of the first prism and then is reflected by the dihedral reflector and eventually hits the tip of the second prism. The two prisms are arranged in such a way that the beam enters and exits each prism in Brewster angle. The dihedral reflector is mounted on a translational rail to adjust the separation between the prisms. The pre-compensated beam is reflected backward with slightly different angle from the input beam. The amount of dispersion induced by the prism pair can be adjusted by changing the distance between the prisms.

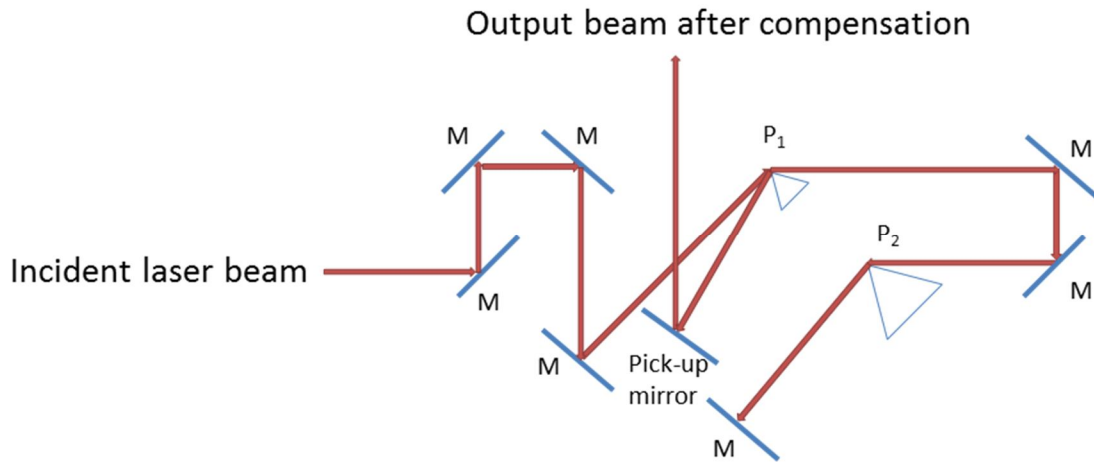


Figure 3.2 Layout of a double-folded prism pair as the dispersion pre-compensation unit.

3.3 Setup for characterizing the propagation properties of fibers

As shown in Fig. 3.3, the laser beam is coupled into a piece of CPCF or HC800-01 and afterwards it is collimated into a parallel beam again. A flipping mirror directs the beam for two separate measurements. (1) For the measurement at the output end of the fibers, the output is measured by an intensity autocorrelator (Femtochrome, FR-103MN) and a spectrometer (Spectral Products, SM442), respectively. (2) The pulse duration needs to be measured at the sample location after focused by the objective lens. In order to achieve it, light after the fiber goes through exact the same optical lenses as in Fig. 3.1, except that the two lenses in the beam

expander are re-arranged. One of them is relocated to a position after the objective lens. Therefore, the laser beam can be re-collimated and directed into the intensity autocorrelator that only works for parallel input beam. This design does not introduce any new lenses and represents the pulse duration in real case of MPM imaging. It should be mentioned that rotated half-wave plate is mounted in the optical path in order to achieve vertical input polarization for the requirement of the autocorrelator.

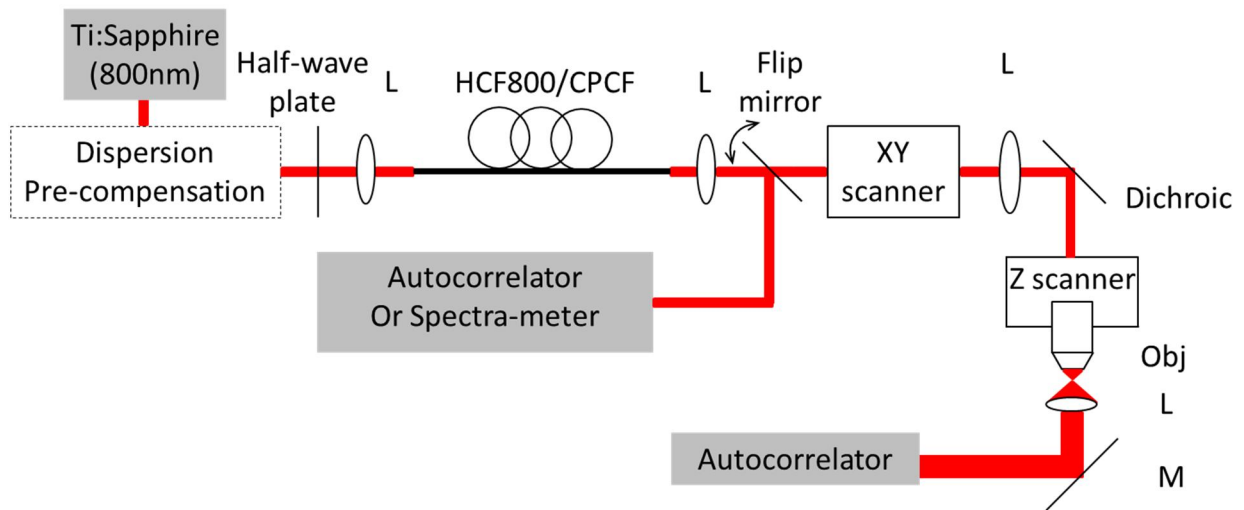


Figure 3.3 The configuration of measuring the fiber properties.

Chapter 4: Characterization of the dispersion of CPCF and HCF

In this chapter, we introduce the theory of dispersion and prism-based dispersion compensation. Two methods to estimate the GVD are provided either based on pulse duration after broadening or based on introduced anomalous dispersion from the prism stretcher. Meanwhile, the autocorrelation as a means to measure the pulse duration is briefly discussed. Then, the GVD of different coupling lenses are calculated, suggesting the proper lenses for the two types of fibers. Moreover, the GVD of the CPCF is characterized by our measurements of pulse durations after the fiber propagation. Due to the dominance by the lenses in the dispersion of the CPCF delivery system, the dispersion of lenses is carefully compensated by prism stretcher. Finally, the pulsewidths after the pre-compensation are measured and discussed for the CPCF. As a comparison, the GVD of HC-800-01 is also calculated and pulse after HC-800-01 propagation is measured after partial pre-compensation.

4.1 Dispersion

The electrical field of a pulse in the frequency domain can be described by [54]

$$E(\omega) = \sqrt{s(\omega)} \exp[-i\varphi_{pulse}(\omega)] \quad (4.1)$$

where $s(\omega)$ is the spectral density (or, the spectrum) of the pulse, and the spectral phase $\varphi_{pulse}(\omega)$ describes the relationship between the frequency components of the pulse. Here, ω represents angular frequency.

When an input pulse $E_{in}(\omega)$ passes through a passive medium (i.e., lenses), the output pulse is given by multiplying a transfer function of the material:

$$E_{out}(\omega) = H(\omega)E_{in}(\omega) \quad (4.2)$$

For a linear passive material, the transfer function is expressed by

$$H(\omega) = \exp[-\alpha(\omega)l/2] \exp[-i\varphi_{mat}(\omega)] = \exp[-\alpha(\omega)l/2] \exp[-ik(\omega)l] \quad (4.3)$$

here, α is loss and for a transparent optical material α is zero; l is the thickness of the material;

the wavenumber (change in spectral phase per unit length) is

$$k(\omega) = 2\pi/\lambda(\omega) = 2\pi n(\omega)/\lambda_0 = \omega_0 n(\omega)/c \quad (4.4)$$

where λ_0 is the wavelength in vacuum, c is the speed of light in vacuum, and ω_0 is angular frequency in vacuum.

To account for dispersion, we expand the wavenumber in a Taylor series:

$$k(\omega) = k(\omega_0) + k_1(\omega_0) * (\omega - \omega_0) + \frac{1}{2}k_2(\omega_0) * (\omega - \omega_0)^2 + \frac{1}{6}k_3(\omega_0) * (\omega - \omega_0)^3 + \dots \quad (4.5)$$

where the terms corresponding to different orders have the following meaning:

$k(\omega_0)$ denotes a constant phase shift;

$k_1(\omega_0) = \frac{dk}{d\omega} = \frac{1}{v_g}$ describes an overall time delay without changing the pulse, and v_g is the

velocity;

$k_2(\omega_0) = d\left(\frac{1}{v_g}\right)/d\omega = \frac{\lambda_0^3}{2\pi c^2} \frac{d^2n}{d\lambda_0^2}$ describes the group velocity dispersion (GVD) per unit

length;

$k_3(\omega_0)$ describes the third-order dispersion per unit length.

Remarkably, GVD and other higher-order dispersion lead to the dispersion. The dispersion temporally broadens a pulse in that different wavelength components travel at different velocities.

If higher-order dispersion terms are neglected, the output pulse for a Gaussian input pulse is given by

$$E_{out}(\omega) = \sqrt{A_\omega e^{-\ln 2(2(\omega-\omega_0)/\Delta\omega)^2}} e^{-ik_2(\omega_0)(\omega-\omega_0)^2 l/2} \quad (4.6)$$

Performing a Fourier transform on equation (4.6), we get $E_{out}(t)$. So intensity is expressed by

$$I_{out}(t) = E_{out}(t) * E_{out}^*(t) = A'_t e^{-4(\ln 2)t^2(\Delta t)^2/((\Delta t)^4 + 16(\ln 2)^2(k_2 l)^2)} \quad (4.7)$$

where Δt means the input transform limited pulse duration.

Comparing to the standard form of a Gaussian pulse, we obtain

$$e^{-4\ln 2(t/\Delta t_{out})^2} = e^{-4(\ln 2)t^2(\Delta t)^2/((\Delta t)^4 + 16(\ln 2)^2(k_2 l)^2)} \quad (4.8)$$

Therefore the output pulse duration is

$$\Delta t_{out} = \sqrt{(\Delta t)^4 + 16(\ln 2)^2(k_2 l)^2}/\Delta t \quad (4.9)$$

where Δt_{out} is the output pulse duration after passing through the optical materials.

The GVD can be calculated from the equation (4.9)

$$k_2 = \sqrt{(\Delta t * \Delta t_{out})^2 - (\Delta t)^4}/(4l * \ln 2) \quad (4.10)$$

The uncertainty principle for the transform limited pulse is given by,

$$\Delta t * \Delta v = C_B \quad (4.11)$$

The time-bandwidth product C_B is a function of pulse profile. C_B is 0.441 for the Gaussian pulse whereas C_B is 0.315 for the Hyperbolic secant pulse. The bandwidth in frequency domain can be converted into the bandwidth in spectral domain by the following relationship

$$\Delta v = c * \Delta \lambda / \lambda_0^2 \quad (4.12)$$

where $\Delta \lambda$ is the spectral bandwidth of the pulse.

Substituting equations (4.11) and (4.12) into equation (4.10), GVD can be expressed by the observables:

$$k_2 = \frac{1}{4l * \ln 2} * \sqrt{(C_B \Delta t_{out} \lambda_0^2 / c \Delta \lambda)^2 - (C_B \lambda_0^2 / c \Delta \lambda)^4} \quad (4.13)$$

where the output pulse duration Δt_{out} can be measured by the autocorrelator, the $\Delta\lambda$ and λ_0 can be measured by the spectrometer for the transform-limited input pulse, material length l can also be measured or known parameter.

In cases where it is hard to define the effective length of the optical medium, $k_2 l$ is defined as the group delay dispersion ϕ_2 (GDD).

In fiber optics, another parameter called the group-velocity dispersion parameter D is commonly used

$$D = -2\pi c k_2 / \lambda^2 \quad (4.14)$$

in the unit of ps/(nm*km).

Noteworthy, D has an opposite sign to k_2 . When $k_2 > 0$, the medium has normal dispersion; otherwise, the medium has anomalous dispersion. In the NIR region, most optical materials have normal material dispersion [55]. Therefore, pulses after passing through the optical medium are spread because the longer wavelength components travel faster than the shorter wavelength components.

4.1.1 Prism-based dispersion compensation

It is well known that prism can separate the ultrashort pulse into its frequency or spectral components since the refractive index of glass depends on frequency. Blue constituent is bent more than red one due to its larger refractive index. If red components experience longer optical path length than blue light after the prism, the broadening pulse can be compressed back. For a prism stretcher we used, we can calculate the induced anomalous dispersion based on the following theory [52].

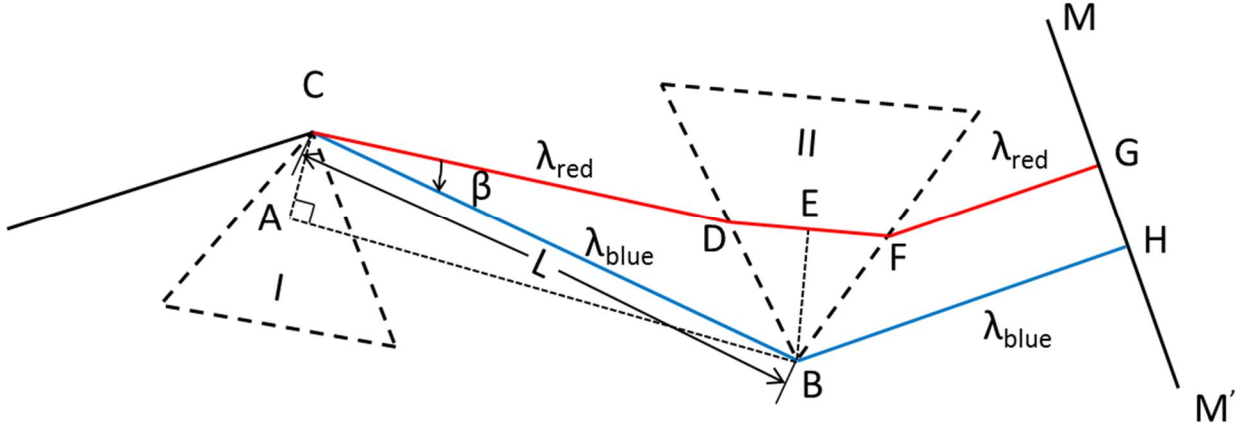


Figure 4.1 Schematic of optical path of double-folded prism pair.

As shown in Fig. 4.1, the optical path length that contributes to the dispersion is given by

$$P = 2 * L * \cos\beta \quad (4.15)$$

where L describes the spacing distance between the apexes of two prisms. β is the dispersing angle after the first prism.

The GDD introduced by the prism compressor can be expressed by

$$GDD_{prism} = \frac{\lambda^3}{2\pi c^2} \frac{d^2P}{d\lambda^2} \quad (4.16)$$

Employing the chain rule for derivatives,

$$\frac{d^2P}{d\lambda^2} = \left[\frac{d^2n}{d\lambda^2} \frac{d\beta}{dn} + \left(\frac{dn}{d\lambda} \right)^2 \frac{d^2\beta}{dn^2} \right] \frac{dP}{d\beta} + \left(\frac{dn}{d\lambda} \right)^2 \left(\frac{d\beta}{dn} \right)^2 \frac{d^2P}{d\beta^2} \quad (4.17)$$

In order to obtain the expressions about $d\beta/dn$ and $d^2\beta/dn^2$, we analyze the light path of prisms in more details as shown in Fig. 4.2.

Using the Snell's law,

$$\sin\phi_1 = n\sin\phi'_1 \quad (4.18)$$

$$\sin\phi_2 = n\sin(\alpha - \phi'_1) \quad (4.19)$$

$$\frac{d\beta}{dn} = -2 \quad (4.26)$$

$$\frac{d^2\beta}{dn^2} = -4n + \frac{2}{n^3} \quad (4.27)$$

Inserting these equations (4.26) and (4.27) into equations (4.16) and (4.17) yield

$$GDD_{prism} = \frac{\lambda^3}{2\pi c^2} * 4L \left[\frac{d^2n}{d\lambda^2} + \left(2n - \frac{1}{n^3} \right) \left(\frac{dn}{d\lambda} \right)^2 \right] \sin\beta - 2 \left(\frac{dn}{d\lambda} \right)^2 \cos\beta \quad (4.28)$$

where n is the refractive index of the prism material at a given center wavelength, $dn/d\lambda$ and $d^2n/d\lambda^2$ are the derivative and second derivative of the refractive index of the material at the same wavelength, respectively. Typically, these parameters can be calculated by the Sellmeier's equation. β can be estimated by

$$\beta \approx -2 \frac{dn}{d\lambda} \Delta\lambda \quad (4.29)$$

When the incident beam size of the pulse that needs to be compressed is considered, we revise the equation (4.28) as

$$GDD_{prism} = \frac{\lambda^3}{2\pi c^2} * \left[4L \left(\frac{d^2n}{d\lambda^2} + \left(2n - \frac{1}{n^3} \right) \left(\frac{dn}{d\lambda} \right)^2 \right) \sin\beta - 2 \left(\frac{dn}{d\lambda} \right)^2 \cos\beta \right] + 4 \left(\frac{d^2n}{d\lambda^2} \right) * 2D_{1/e^2} \quad (4.30)$$

where D_{1/e^2} is the beam diameter of incident laser pulse at $1/e^2$.

According to the above derivations, a certain amount of anomalous dispersion from the prism pair can be calculated based on three hypotheses. Firstly, all the light exited from the prism I can travel through the prism II. Secondly, prisms are used at minimum deviation and Brewster's angle incidents and exits at each surface of prisms. Thirdly, the insertion of the second prism is fixed where the shortest wavelength component hits the tip of the second prism.

In our experiment, the diameter of the laser beam is measured by the CCD camera ($D_{1/e^2}=3\text{mm}$). The spectrum of laser at different pre-compensation cases can be measured to obtain λ and $\Delta\lambda$. The refractive index of the SF10 prism material can be expressed by Sellmeier's equation

$$n^2 = 1 + \frac{B_1\lambda^2}{\lambda^2 - C_1} + \frac{B_2\lambda^2}{\lambda^2 - C_2} + \frac{B_3\lambda^2}{\lambda^2 - C_3} \quad (4.31)$$

where $B_1=1.62153902$, $B_2=0.256287842$, $B_3=1.64447552$, $C_1=0.0122241457 \mu\text{m}^2$, $C_2=0.0595736775 \mu\text{m}^2$, $C_3=147.468793 \mu\text{m}^2$.

Thus, the $dn/d\lambda$ and $d^2n/d\lambda^2$ can be derived from the equation (4.31). The separation L between the apexes of the prism pair can be recorded from the experiments.

Assuming the Brewster's angle incidence, the introduced anomalous dispersion from prism pair could be estimated by substituting all above known parameters into equation (4.30).

4.1.2 Intensity autocorrelator as a measurement of pulse duration

Pulse duration can be measured by an intensity autocorrelator [57-59]. In order to clarify the following pulse measurement, we firstly introduce the concept of intensity autocorrelation. The ultrashort-pulse laser employed in MPM imaging usually produces pulses on the order of several tens of femtoseconds in time duration. Based on the Nyquist theorem, minimum sampling frequency should be at least twice the highest frequency in the signal to avoid aliasing. However, no photo-detector is fast enough to measure femtosecond pulses. Therefore, autocorrelation is usually used to measure ultrashort pulses.

Figure 4.3 describes the schematic of an intensity autocorrelator. The parallel laser beam is split into two arms. One arm is fixed and the other can vary the delay path-length relative to the

fixed arm. Therefore a delay time $\tau = 2\Delta x/c$ emerges, where Δx is the shift of the adjustable arm, and c is the speed of light. Then the two non-collinear beams are spatially overlapped inside a SHG crystal that produces a frequency-doubling signal. This signal is recorded by a slow detector, which is given by:

$$I_M(\tau) = \int_{-\infty}^{+\infty} I(t)I(t - \tau)dt \quad (4.32)$$

where $I(t)$ is the intensity of the fixed beam, $I(t - \tau)$ is the intensity of the delayed beam, and τ is the delay time. Only when the two beams are spatially focused into the same point in the SHG crystal and the time delay is within the coherence length of the laser, autocorrelation trace from the SHG signal will emerge. Otherwise, no SHG signal is generated.

The pulse duration in time domain can be estimated in view of the recorded autocorrelation trace. The conversion factor from FWHM of autocorrelation trace (ΔT) to FWHM of pulse duration (Δt) depends on the pulse shape. The conversion factors ($\Delta t/\Delta T$) for the Gaussian pulse and Hyperbolic Secant pulse are 0.707 and 0.648, respectively. If the pulse shape is known or assumed, the pulse duration can be measured. However, the phase information of the pulse is lost in the intensity autocorrelation.

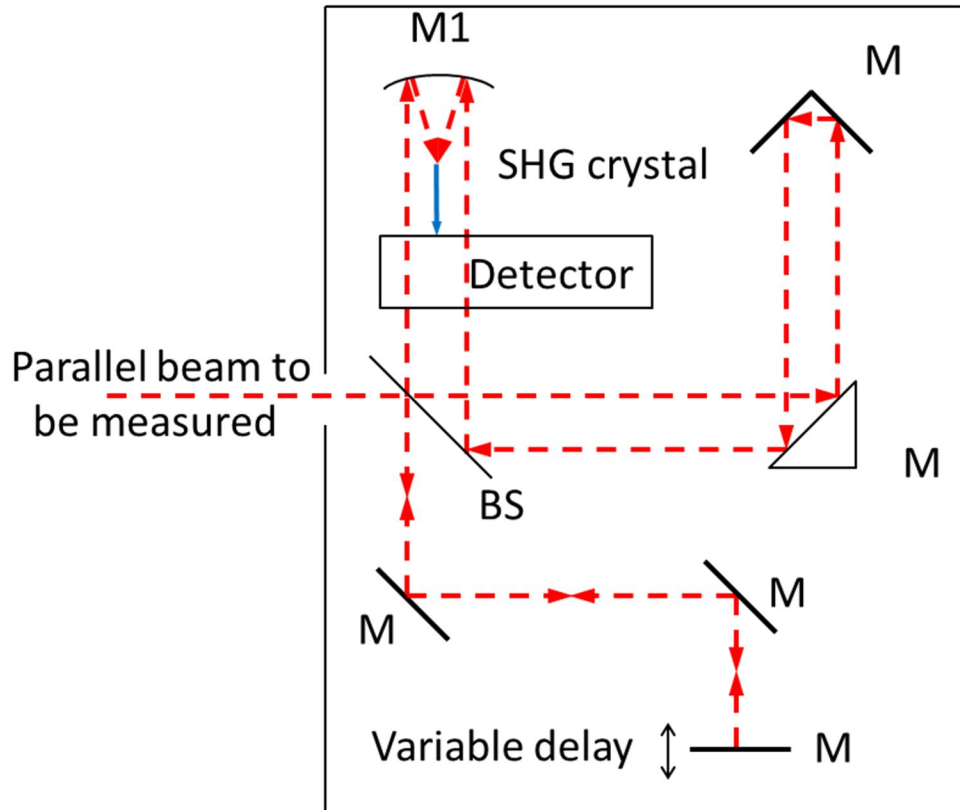


Figure 4.3 Principle of intensity autocorrelation.

4.2 Pulse broadening due to dispersion from various lenses

The coupling components are indispensable for fiber-delivered system and they can introduce relatively large dispersion. Moreover, remarkable dispersion dominated by the 40X objective lens makes pulse broadening even worse [60, 61]. Except the essential 40X objective lens for multiphoton imaging, the coupling elements can be substituted by other thinner lenses to further reduce unnecessary pulse stretching. Thus, several combinations of thinner lenses are firstly measured by the intensity autocorrelator. Then, the GDD of the various lens combinations can be calculated from the equation (4.13). For each combination, we also utilize the prism stretcher to compress the pulse and record the corresponding prism separations and locations

where the second prism inserts. Finally, the induced anomalous GDD from prism pair can be estimated based on the formula (4.30). All results are summarized in Table 4.1.

Clearly, the Edmund spherical lens and Newport 5X are suitable for CPCF because of low dispersion and matching NA. For HC-800-01, the alternative Newport10X and 5X are better to match high NA. Moreover, the GDD of lenses are calculated based on the pulse broadening, suggesting that lenses with higher NA typically introduce larger GDD. Furthermore, the induced anomalous GDDs from the prism pair are estimated for each case when we assume that our prism setup satisfies all the three premises of the theory.

In table 4.1, the estimated anomalous GDD based on the theory of the prism pair is much higher than the calculated normal GDD of the lenses by the measurement of the pulsewidth. The discrepancy possibly stems from the following two aspects. Firstly, the second prism in our setup is not big enough to capture all the dispersed wavelengths from the first prism, losing some wavelength components at the edge of the wavelength band. Also the condition that the shortest wavelength component hits the tip of the second prism may not be fully satisfied. Secondly, the Brewster-angle incidence and exit may not be aligned precisely at each surface of the prisms. If the incident angle is larger than the Brewster-angle, the dispersing between the red (longer wavelength) and blue (shorter wavelength) components would be reduced and thus less anomalous dispersion could be introduced by the prisms [62, 63]. Based on the equations (4.16) and (4.17), we simulate the effect of the incident angle and center wavelength on the introduced anomalous dispersion by prism pair at a certain separation, and the results are shown in Fig. 4.4. In Fig. 4.4, the introduced GDD at 65° is only half of that at Brewster-angle incidence (59.6°). Therefore, the introduced anomalous GDD varies significantly even when a small angle difference is occurred. Our simulation also shows that the introduced GDD varies with the center

wavelength. On the whole, the estimated anomalous dispersion based on the theory of the prism pair for ideal conditions may not be accurate for the real experimental conditions.

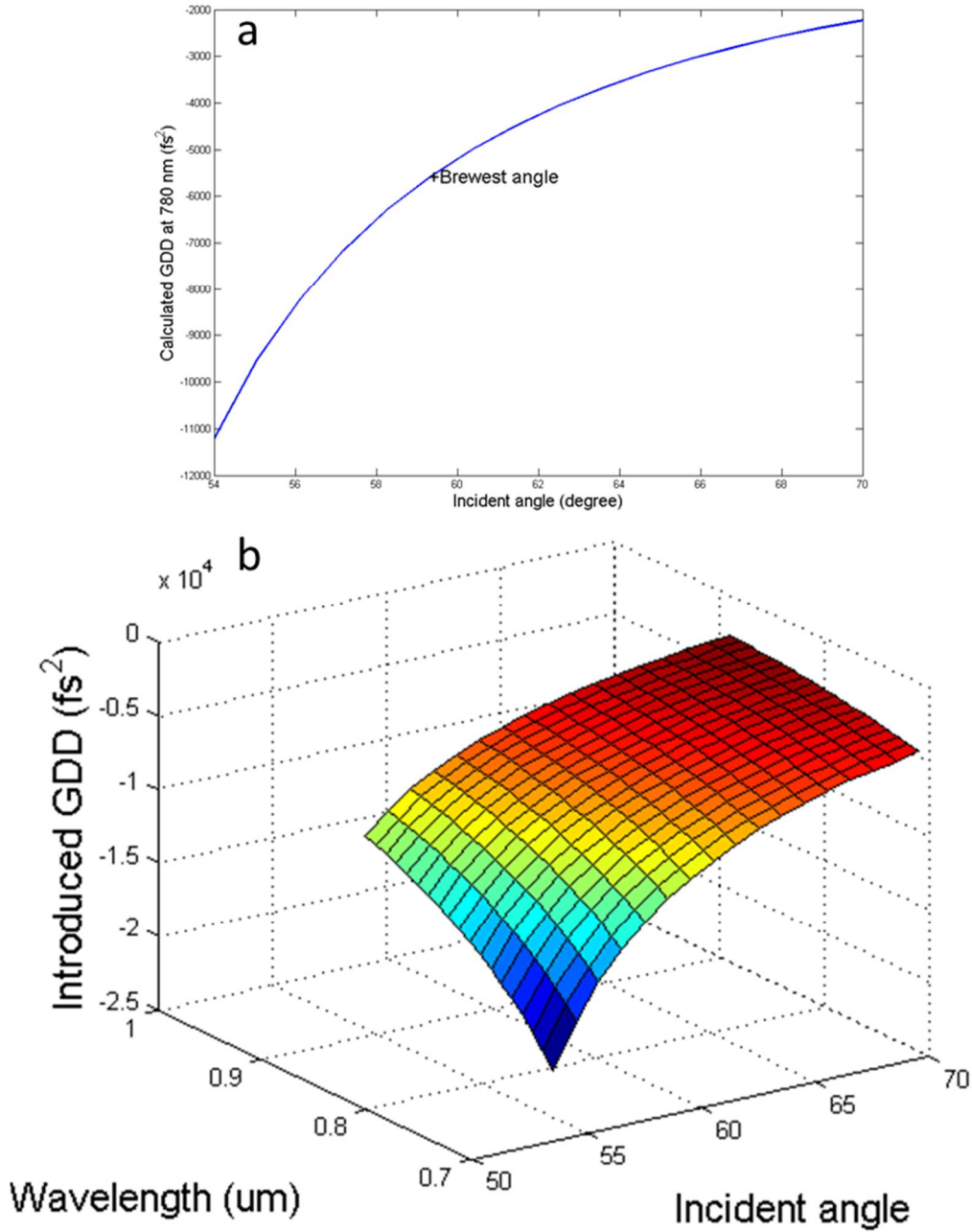


Figure 4.4 Calculated GDD introduced by the prism pair. (a)The relationship between introduced anomalous GDD and incident angle of prism at the 780 nm at the specific prism separation; (b) 3D plot of GDD when both incident angle and wavelength vary.

Table 4.1 Pulsewidth of various lens combinations without and with pre-compensation

Lens combination	Olympus 4X (NA 0.1) and Olympus 10X (NA 0.3)	Newport5X (NA 0.1) and Newport 10X (NA 0.25)	Spherical lens (NA 0.027) and Newport 5X (NA 0.1)	Spherical lens, Newport 5X, scan and tube lenses, and Olympus 40X
Pulsewidth without compensation	230 fs	120 fs	51 fs	288 fs
Calculated GDD from pulsewidth	820 fs ²	420 fs ²	180 fs ²	1000 fs ²
Pulsewidth after prism compensation	28.9 fs	19.4 fs	19.3 fs	20.2 fs
Corresponding prism spacing /insertion	29 cm /13.5 mm	12 cm /11.5 mm	11 cm /11 mm	28 cm /10.5 mm
Calculated anomalous GDD from prism pair	-5600 fs ²	-1800 fs ²	-1600 fs ²	-5300 fs ²

According to the definition of GVD and GDD in Section 4.1, the GDD of the lenses can be estimated based on their thickness and material,

$$GDD_{material} = l * \frac{\lambda^3}{2\pi c^2} * \frac{d^2 n_m}{d\lambda^2} \quad (4.33)$$

For instance, the spherical lens (Edmund 69-476) is ~ 2 mm thick in the center. The scan lens (Thorlabs LA1509B) is ~ 3.6 mm thick and tube lens (Thorlabs LA1708-B) is ~2.8 mm thick. Newport 5X (M-5X) is ~ 2.7 mm thick. The substrate of these lenses we used is N-BK7. The thickness and material of the objective lens (Olympus 40X) are unknown. However, from literature, the GDD of a typical 40X objective lens at 780 nm has been found to be ~950 ±100 fs² [53, 60].

In the Sellmeier's equation (4.31), the coefficients of N-BK7 are B₁=1.62153902, B₂=0.256287842, B₃=1.64447552, C₁=0.0122241457 μm², C₂=0.0595736775 μm² and C₃=147.468793 μm². At the 780 nm wavelength, we obtain

$$\frac{d^2 n_{BK7}}{d\lambda^2} = 0.05546 \text{ } \mu\text{m}^{-2}$$

For the lens combination in the last case in table 4.1, the estimated material dispersion is found to be $GDD_{lensesmaterial} \approx 1400 \text{ fs}^2$, which includes all the above mentioned lenses. This result indicates that the calculated GDD (1000 fs²) based on the broadening of pulse duration approaches the estimation obtained from material thickness.

4.3 Characterization of the dispersion of CPCF

4.3.1 Assessment of GVD without pre-compensation

The autocorrelation traces without dispersion compensation for different cases are shown in Fig. 4.5. Assuming a sech² pulse shape, the pulsewidth of the laser is estimated to be ~14 fs. In

order to study the dispersion of a CPCF, the dispersion introduced by the coupling lens and the collimation lens needs to be taken into account and is thus separately measured by the autocorrelator. Here, two objective lenses (Olympus, Plan N 4X NA=0.1 and MPlanFL 10X NA=0.3) are employed as the coupling and collimation lenses. The red line shows that the pulse is stretched to ~230 fs after these two objective lenses. Then a piece of 40 cm length of CPCF is inserted between the coupling lens and the collimation lens. After the CPCF delivery, the green line indicates a ~246 fs pulsewidth with the output pulse energy of 1.25 nJ. Figure 4.5 clearly reveals that the pulse is only slightly further broadened after inserting the CPCF, which demonstrates the extremely low dispersion of CPCF in the transmission window.

According to the previously derived relationship between the pulse duration and experienced GDD, we can make estimation on the dispersion parameter of the fiber. In our case, the original transform-limited pulses have 91 nm bandwidth at the center wavelength 780 nm ($\Delta\lambda=91$ nm, $\lambda=780$ nm). Assuming the second-order dispersion is dominate, we obtain the GDD arising from the lenses φ_{lenses} by substituting the output duration (230 fs) into equation (4.13). Similarly, the GDD from both CPCF and lenses can be calculated based on the output duration (~246 fs). Then

$$\varphi_{CPCF} = \varphi_{CPCF+lenses} - \varphi_{lenses} \quad (4.21)$$

By this method, the GVD of the CPCF is calculated as about 140 fs²/m. This estimation of dispersion parameter for CPCF is on the same order as the value quoted in Ref [10], which confirms the measurement results.

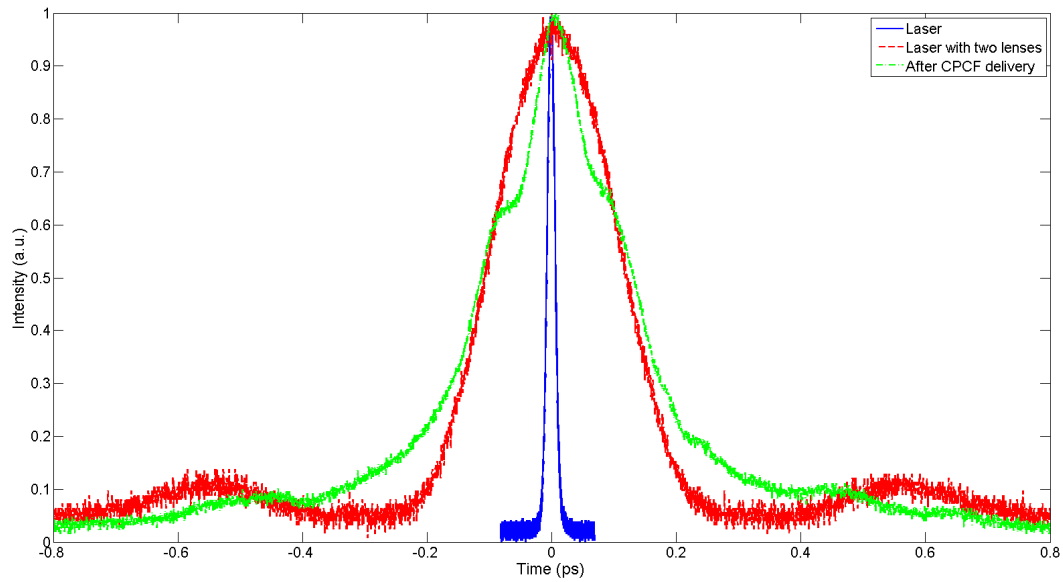


Figure 4.5 Intensity autocorrelation measurements for different cases without the dispersion compensation. The blue curve shows the pulse direct from laser output; the red line shows the laser pulse after passing through the coupling and collimation lenses; The green line shows the pulse after passing through the CPCF in addition to the coupling and collimation lenses.

4.3.2 Pulses with different fiber length under dispersion pre-compensation

From Fig. 4.5, one could deduce that the dispersion from CPCF is significantly smaller than that of the objective lens employed. Therefore, the dispersion from the objective lens and other optical components should be compensated for further enhancement of the MPM signal intensity. A short length (40 cm) of a CPCF is initially chosen on account of the relatively high loss.

4.3.2.1 Autocorrelation trace of a CPCF with short length

Figure 4.6 illustrates the autocorrelation traces measured with or without the CPCF when dispersion pre-compensation unit is applied. We use the configuration described in Fig. 3.3 to make this measurement. In Fig. 4.6(a), the pulse is measured at the sample location with all the optical components of the imaging microscope, including a piece of the CPCF with 0.4 m length. The pulse at the sample location can be fully compressed down to 34.8 fs, however, with strong satellite peaks in the autocorrelation trace. Furthermore, we observed that the alignment of the prism pair could strongly affect the relative intensities and locations of the satellite peaks. The distribution of satellite peaks is not related to the polarization direction of incident beam. In order to investigate the possible origin of these satellite peaks, the pulse duration at the CPCF end without entering the microscope is measured and shown in Fig. 4.6(b). Compared to results shown in Fig. 4.6(a), Figure 4.6(b) describes the pulse measurements in which the dispersion from the multiphoton imaging sub-system is excluded and pre-compensation is only applied to minimize the pulse at the fiber end. When near optimal pre-chirping is employed, the pulse at the 0.4m CPCF output is compressed back to 34.9 fs with some satellites peaks. Again, the intensities and locations of the satellites peaks change with the variation of the prism separation. At the same prism separation, similar autocorrelation traces can be readily reproduced. Here, we wonder whether the laser itself works in an unstable status or not due to possible reflection. To verify it, the pulse is measured again at the sample location using the same setup as used in Fig. 4.6 (a), except that the 0.4m-long CPCF is removed. This result is shown in Fig. 4.6(c). It reveals clean autocorrelation trace without satellites and the pulse is compressed down to 17.8 fs with optimal pre-compensation. In consequence, this satellite phenomenon is determined to come from the CPCF.

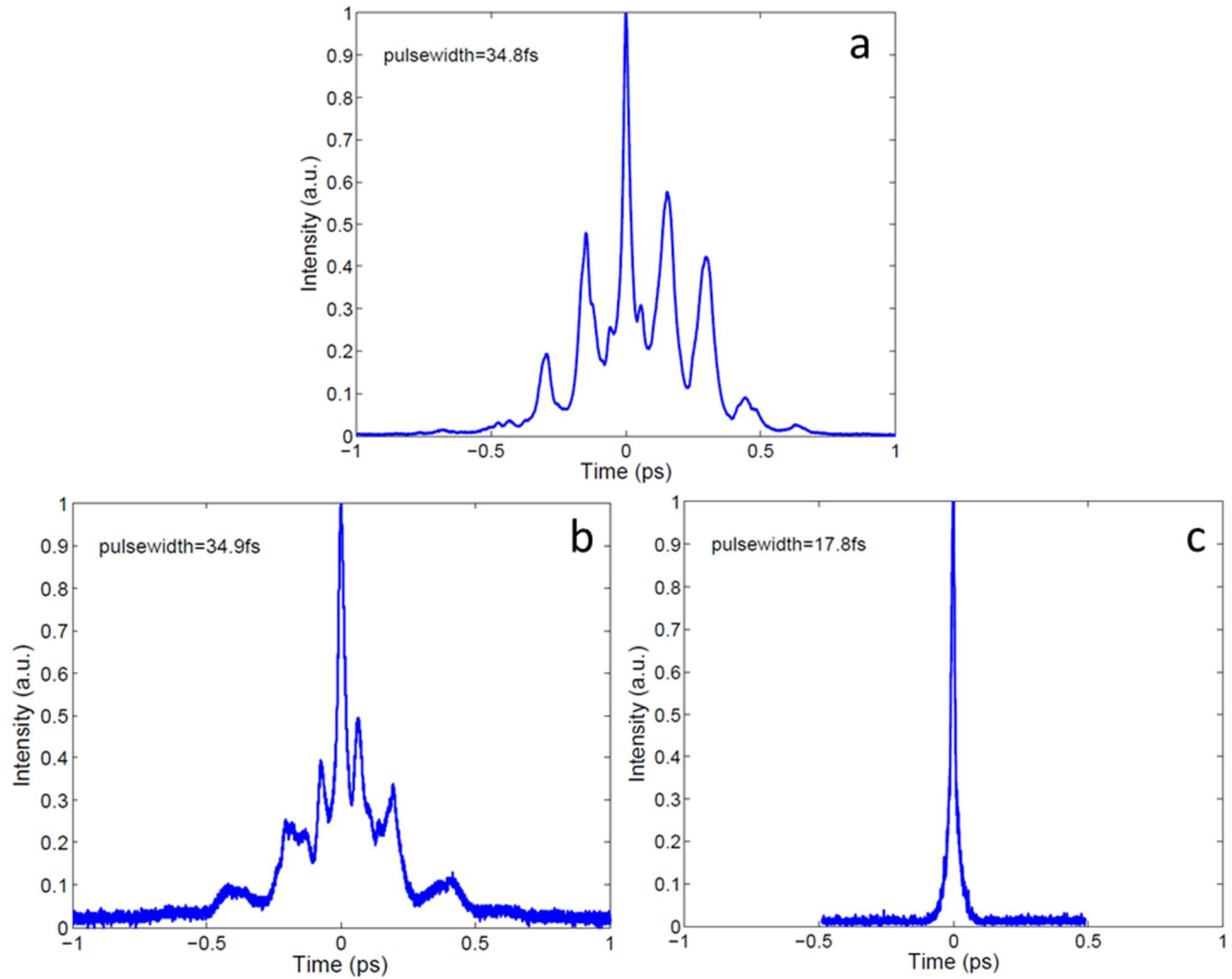


Figure 4.6 Intensity autocorrelation measurements of a 0.4 m CPCF and laser itself with optimal dispersion compensation. (a) Autocorrelation at the sample location with all optical elements including the 0.4 m CPCF. The pulse on the sample is compressed back to 34.8 fs. (b) Autocorrelation at the end of the 0.4 m CPCF. The pulse at the fiber end is compressed back to 34.9 fs. (c) Autocorrelation at sample location with all the optical elements except the CPCF. The pulse on the sample is compressed down to 17.8 fs.

4.3.2.2 Autocorrelation trace of a CPCF with longer length

In order to examine whether modal dispersion could be accounted for the observed satellite phenomenon, another longer piece of CPCF with 1.2 m length is utilized to replace the 0.4 m

long CPCF. The exact same configuration is used as previously, except the CPCF has a longer length. Figure 4.7 shows the pulse measured at the sample location after passing through the 1.2m CPCF and the MPM imaging sub-system. A much cleaner pulse is obtained and the pulse is compressed down to ~ 20 fs. Consequently, the CPCF enables delivering of sub-30 fs pulses through the fiber to tissue samples and hence can potentially increase the MPM excitation efficiency compared with pulses longer than 100 fs.

Comparing Figs. 4.6 and 4.7, the satellite phenomenon is significantly suppressed when a longer CPCF is used. This suggests that the spatial mode of the beam is not pure single mode and some residual higher-order spatial modes co-exist when a short (e.g. 0.4m) CPCF is used. The satellite phenomenon is likely caused by the residual higher-order spatial modes. When the fiber length is increased, the higher-order spatial modes are attenuated quickly and eventually vanish. This is also confirmed by the spatial mode pattern measurement described in Chapter 2. Thus, the CPCF requires a sufficient transmission length to suppress other higher-order modes. In consideration of the attenuation of the CPCF, different lengths of the CPCF are tested. Our results show that a CPCF length of ~ 0.8 m is sufficient to ensure a single mode transmission.

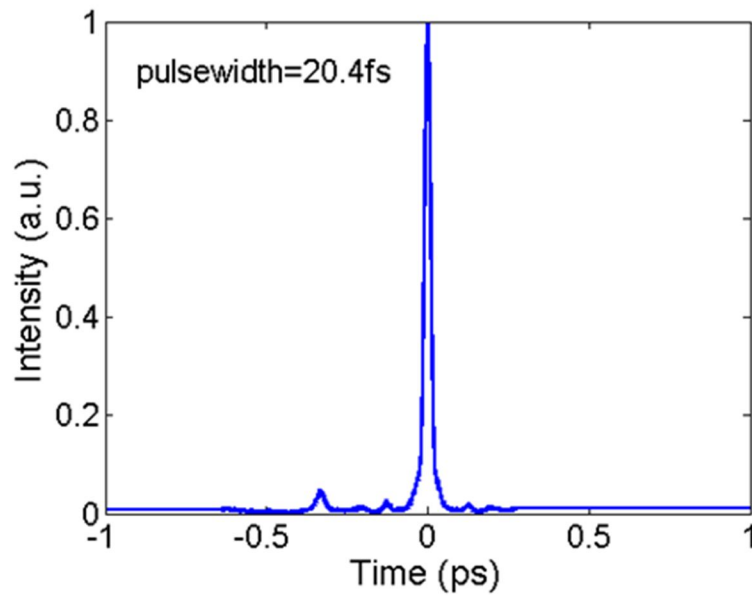


Figure 4.7 Intensity autocorrelation measurements of the 1.2m CPCF at sample location with optimal dispersion compensation. Autocorrelation includes all optical components and the 1.2m CPCF. The pulse on the sample is compressed back to 20.4 fs.

4.4 Comparison with the dispersion characterization of HC-800-01

4.4.1 Assessment of GVD without pre-compensation

To compare the dispersion property of CPCF with commercial HCF, next, the CPCF is replaced by a piece of HC-800-01 of 0.4 m length. As we mentioned in Section 4.2, the Newport10X and 5X lenses are chosen as the coupling elements to match with the higher NA of the HC-800-01. Without prism compressor, the pulse that is transmitted to the fiber tip by the HC-800-01 is severely stretched to 2,000 fs [Fig. 4.8]. This broadening arises from the dispersion of the HC-800-01 and the coupling lenses used in the system.

Similarly, the GVD of the HC-800-01 can be calculated as $17,000 \text{ fs}^2/\text{m}$ based on the equation (4.13). The corresponding group-velocity dispersion parameter D is obtained as follows:

$$D = -\frac{2\pi c}{\lambda^2} k_2 = -50 \text{ ps/nm} \cdot \text{km}$$

The estimated D of the HC-800-01 closely matches with the average value acquired from dispersion curve of the HC-800-01 [Fig 2.4(b)].

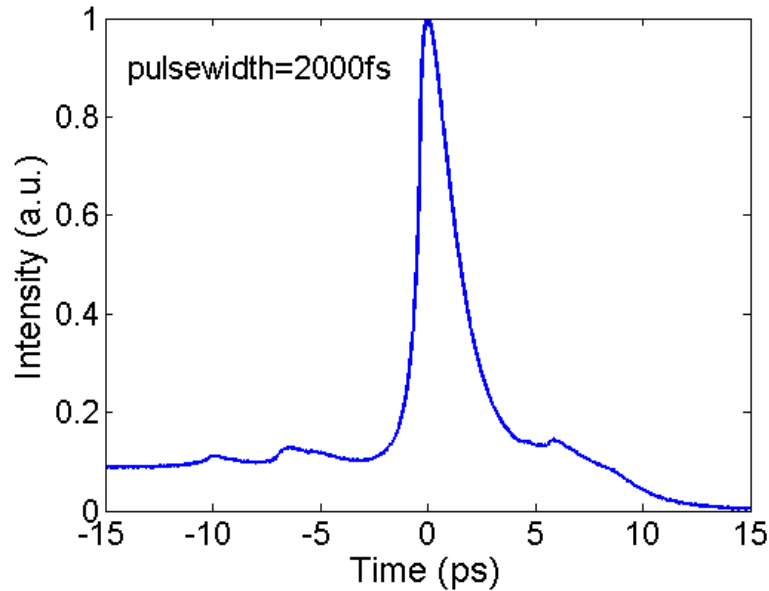


Figure 4.8 Autocorrelation trace of the 0.4 m HCF at fiber tip without pre-compensation. The coupling and collimation lenses are included, plus one piece of HC-800-01 with 0.4 m length. The pulse after the HCF transmission is approximately 2000 fs.

4.4.2 Autocorrelation with pre-compensation

To check whether pulse delivered by the HC-800-01 could be fully compensated by prism compressor, the pulses at the fiber output end are continuously measured when the prism separation and insertion are optimized. Unfortunately, the observed narrowest pulsewidth is around 400 fs even for a very short HC-800-01 with 10 cm length [Fig. 4.9]. We attribute the limited compression to the somewhat large GVD at 780 nm, large bandwidth of pulses, and dramatic third order dispersion of HC-800-01.

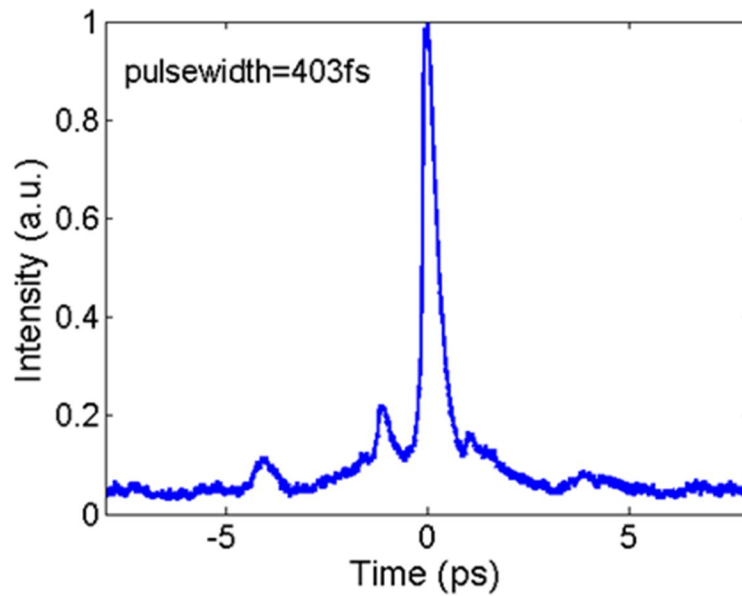


Figure 4.9 Autocorrelation trace of the 0.1 m HCF at the fiber end under the pre-compensation. The pulse at the fiber output is compressed down to 403 fs.

The above analysis clearly reveals that the prism compressor cannot fully compress the pulses after propagating through a HC-800-01 even with 0.1 m length. Moreover, a 0.1m-long HC-800-01 is too short for the MPM imaging. So the HC-800-01 with 0.4 m length is chosen for the following experiments. In this case, the pulsewidth at the sample location under pre-compensation is shown in Fig. 4.10. The pulse on the sample is compressed down to approximately 700 fs.

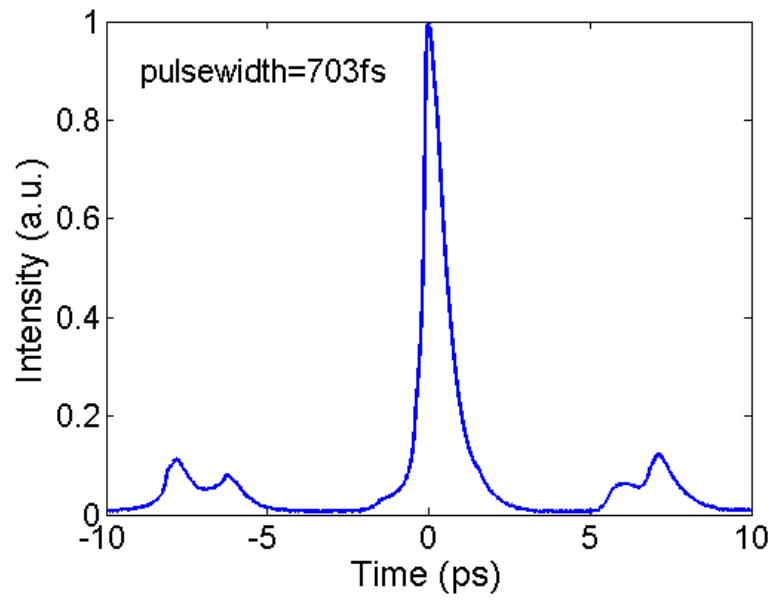


Figure 4.10 Autocorrelation trace of the 0.4 m HCF at sample location with pre-compensation. All optical components are included, plus one piece of HC-800-01 with 40 cm length. The pulse on the sample is compressed to 703 fs.

Chapter 5: System image demonstration

The appealing performance of CPCF applied in the MPM imaging is evaluated and validated by multiphoton images of different samples. As a comparison, MPM imaging is also implemented with light delivered by HC-800-01. All the images are acquired by employing the imaging system depicted in Fig. 3.1. Meanwhile, the length of the CPCF is chosen to be ~ 0.8 m to maintain single mode transmission while the length of the HC-800-01 is chosen to be ~ 0.4 m to maintain a reasonable dispersion. The laser power on the sample is kept the same for the two fiber-delivery configurations. Moreover, the images are typically acquired at 2.6 s per frame, corresponding to 10 μ s dwell time per pixel. As a default condition, the above dwell time or integration time per pixel is generally used in the following experiment. If the integration time is altered, we deliberately describe it. Furthermore, the gain setting in PMT is recorded and remains unchanged to make a fair comparison. In the subsequent images in false color, red denotes TPEF channel and green denotes SHG channel.

5.1 Imaging biological samples based on fiber-delivered system

Figure 5.1 compares the TPEF images of Yew leaf based on light delivery by the CPCF and the HC-800-01, respectively. Although unstained samples usually require high light intensities in order to excite MPM signals, the bright images of leaf appear even at relatively low power on the sample (~ 4 mW). In Fig. 5.1(a), the autofluorescence from the stomata (holes in a leaf) and papillae on the leaf surface are observed in a well-organized pattern. In contrast, the signals in Fig. 5.1(b) are faint even when power on the sample is increased to 6 mW after HC-800-01 fiber delivery.

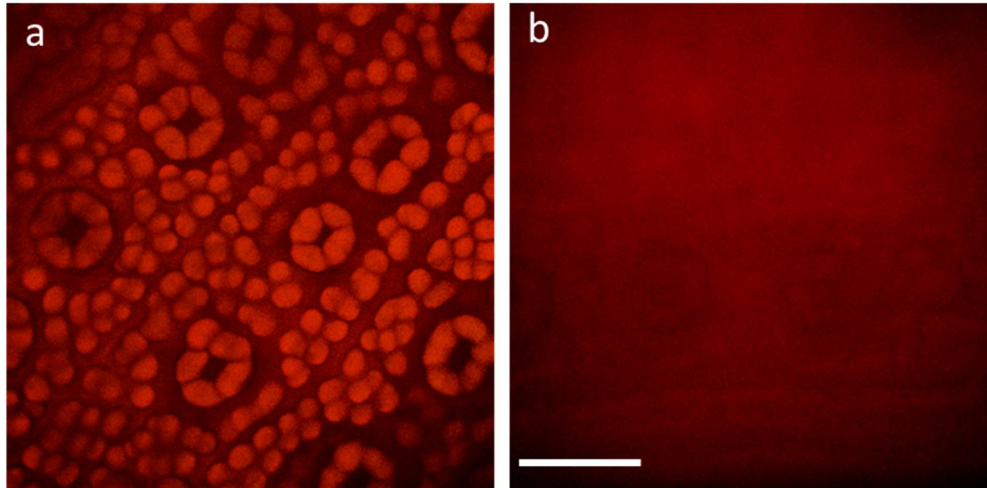


Figure 5.1 MPM images for Yew leaf based on two fiber-delivery systems. (a) the power delivered by 0.8 m CPCF on the sample is about 4 mw; (b) the power delivered by a 0.4 m HC-800-01 on the sample is about 6 mw. Integration time per pixel for both images is 10 μ s; the scale bar is 50 μ m.

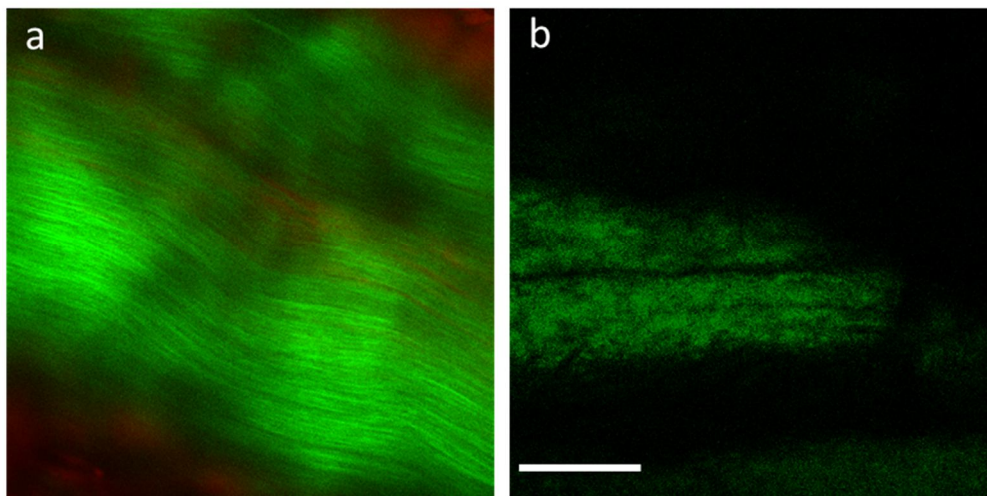


Figure 5.2 MPM images for rat-tail tendon based on two fiber-delivery systems. (a) The power delivered by 0.8 m CPCF on the sample is about 4 mw; Integration time per pixel is 10 μ s; (b) the power delivered by a 0.4 m HC-800-01 on the sample is about 4 mw; Integration time per pixel is 30 μ s. The scale bar is 50 μ m.

In Fig. 5.2, SHG images of rat-tail tendon are acquired by light delivery by the CPCF and the HC-800-01, respectively. In Fig. 5.2(a), fine collagen fibrils within the collagen bundles can

be clearly resolved. The SHG image of rat-tail tendon is consistent with its general structure that Type I non-centrosymmetric collagen is dominant inside the tendon. For comparison, the corresponding tendon images are obtained with HC-800-01 fiber delivery in Fig. 5.2(b). Although pixel dwell time is tripled, SHG signals are much weaker with obscure details of the structures for the tendon.

5.1.1 Imaging human skin based on fiber-delivered system

As shown in Fig. 5.3, human skin consists of two typical layers, epidermis and dermis. The outermost layer, epidermis, has several sub-layers including stratum corneum (SC), stratum granulosum (SG), stratum spinosum (SS), and stratum basale (SB). The SB creates new cells in the epidermis layer. Then living cells continuously migrate outwards through SS and SG. In this process, cells mature which results in larger size and lower density. Eventually, cells become dead in the SC layer and peel off. The deeper layer called dermis is made up of extracellular matrix structures such as collagen and elastin. Skin as a highly scattering organ poses a big challenge for *in vivo* imaging by traditional confocal microscopy [64]. However, MPM is a promising tool since it acquires intrinsic contrast from tissue without staining and it has deep penetration depth provided by NIR [65, 66].

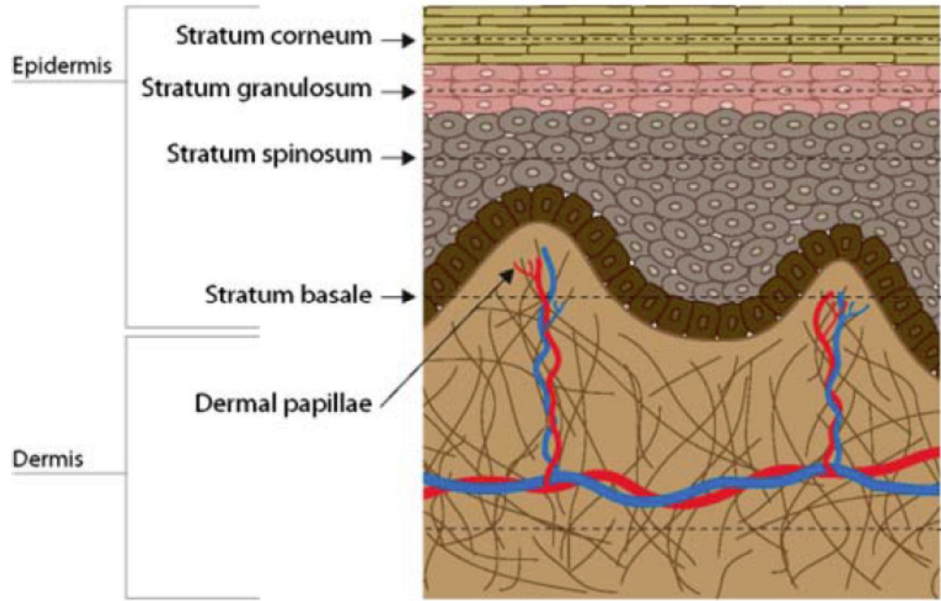


Figure 5.3 Anatomy of human skin [67].

Figure 5.4 shows the merged TPEF/SHG images of the right forehead skin of a 68 year old female based on the CPCF light delivery. The power delivered by the CPCF on the fresh skin sample is about 5 mW. In Fig. 5.4, MPM images are acquired at different depths from the surface to deeper part of the skin. Figure 5.4(a) shows the bright fluorescence signals with no definite shape in the SC layer where Keratin as endogenous fluorophore is substantially accumulated. The larger cells in SG are partially overlaid by signals from SC [Fig. 5.4(b)]. In contrast, relatively small cells in SS are clearly revealed in Fig. 5.4(c)-(d). Interestingly, the donut-shaped cytoplasm of cells in SG and SS produces strong TPEF signals. The reason is that NADH provides autofluorescence in the cytoplasm whereas nuclei show no fluorescence. In Fig. 5.4(e), dense and smaller cells in SB are displayed simultaneously with collagen indicated by green SHG contrast, which presents the junction between epidermis and dermis. The deep

location in dermis layer is revealed by strong SHG from collagen and relatively weak TPEF from elastin fibers [Fig. 5.4(f)].

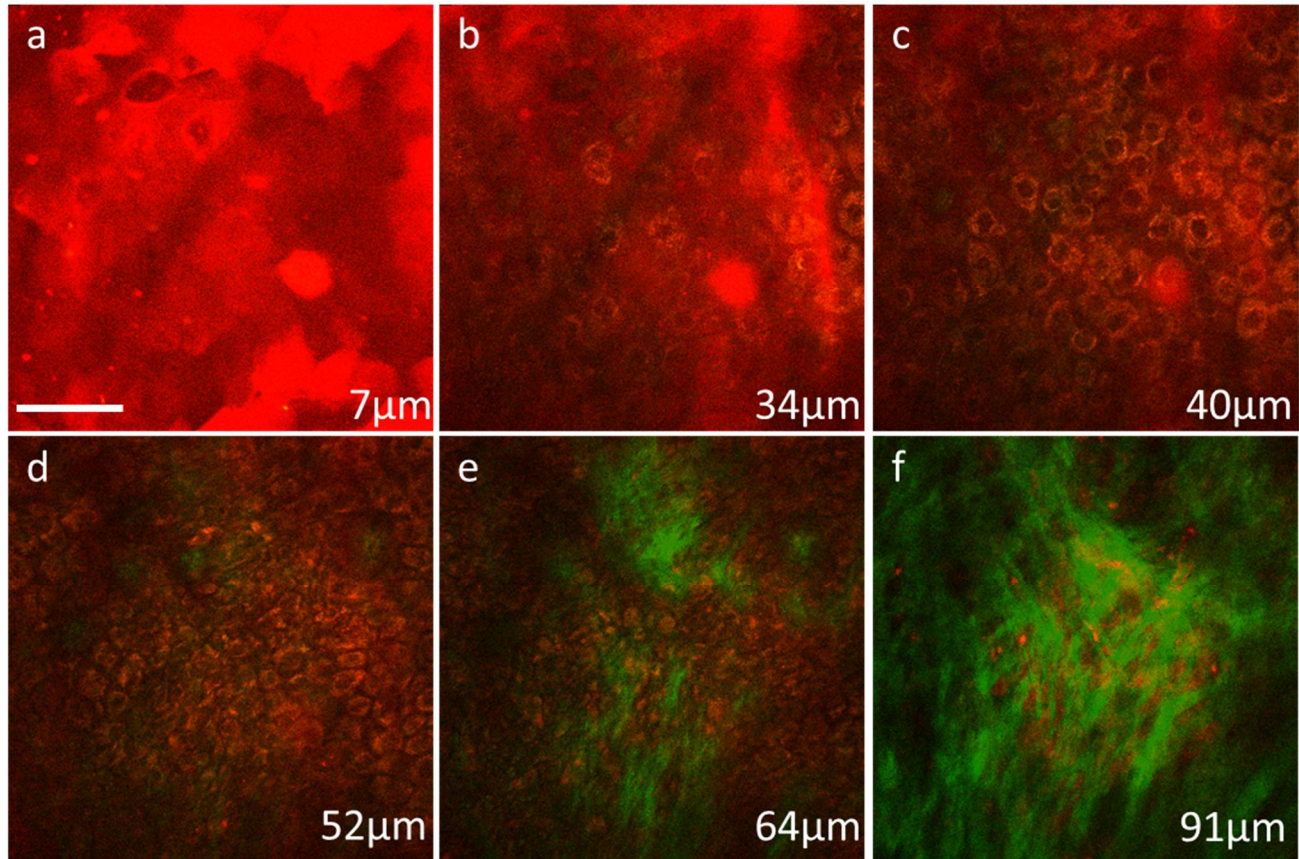


Figure 5.4 MPM images of human skin when power delivered by 0.8 m CPCF on the sample is 5 mw; The integrated images are arranged from outmost layer to deeper layer of skin. The number on each image denotes the distance of current image from the top surface. Integration time per pixel for all images is 10 μ s. The scale bar is 50 μ m.

Fig. 5.5 shows the corresponding skin images acquired with the light delivered by the HC-800-01 with the same power on the sample. Although the pixel dwell time is extended to 30 μ s, the structure from each layer in human skin cannot be visualized clearly. We attribute it to the low excitation efficiency because the HC-800-01 broadens the pulse dramatically.

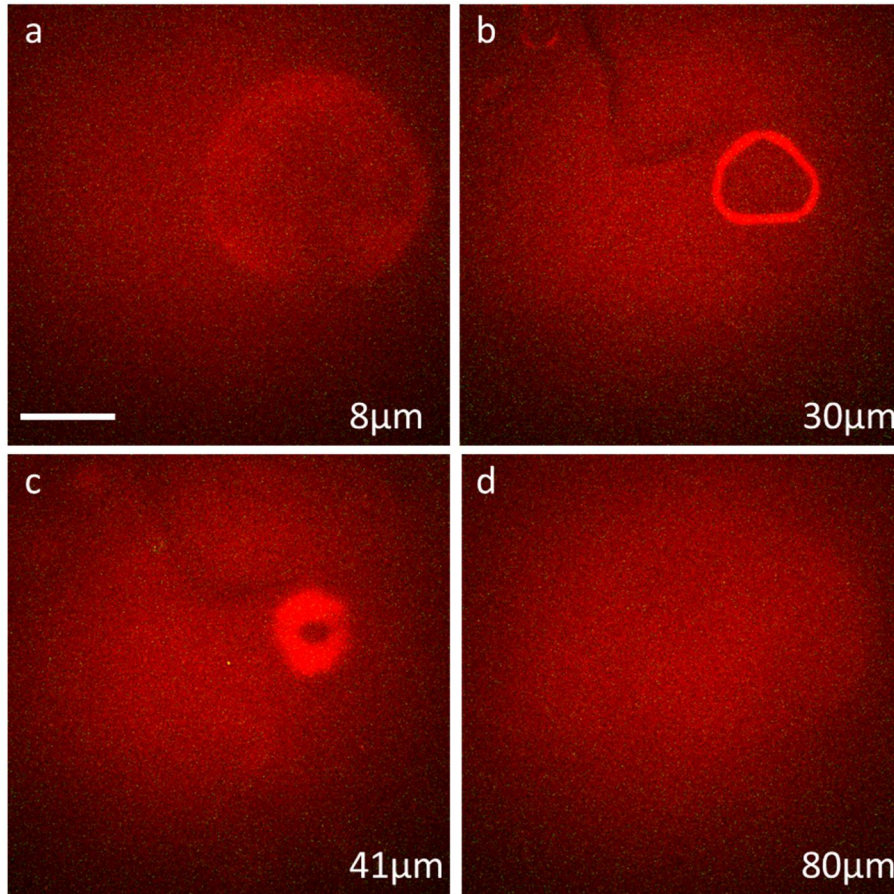


Figure 5.5 MPM images of human skin when power delivered by the 0.4 m HC-800-01 on the sample is 5 mw; The number on each image denotes the distance of current image from the top surface. Integration time per pixel for all images is 30 μ s. The scale bar is 50 μ m.

The strong TPEF, possibly from NADH in the cellular layer, is clearly revealed by employing the 0.8 m CPCF. No apparent TPEF signals can be observed by using the 0.4 m HC-800-01. The dramatic enhancement is possibly attributed to shorter pulses and an extended bandwidth towards shorter wavelength enabled by the CPCF. The extended bandwidth of the CPCF is beneficial for increasing the two-photon fluorescence signals for fluorophores (e.g.

NADH, DAPI, etc.), which have two-photon absorption peaks between 700 to 730 nm as describer in Chapter 2. This short band is fully supported by CPCFs, but not by the HC-800-01.

5.1.2 Imaging human tooth based on fiber-delivered system

As illustrated in Fig. 5.6, enamel, dentin, pulp tissue, and cementum constitute the essential components of the human tooth. Among them, enamel and dentin are two major layers. The top layer, enamel, is the most mineralized layer in the body. The main mineral called hydroxyapatite forms enamel prisms or rods with the diameter of 4~6 μm . In enamel, no collagen exists. Dentin is a connective tissue that lies between enamel and pulp tissue. Dentin is less mineralized and less brittle than enamel. The porous dentin, with main organic constituent of fibrous collagen, is structured with dentin tubules that radiate from pulp cavity to enamel. The diameter of dentin tubules is larger near the pulp cavity and then gradually deceases outward. Other researchers have demonstrated that enamel generates autofluorescence in the wavelength region of 400~600 nm [68] and dentin offers strong SHG [69, 70].

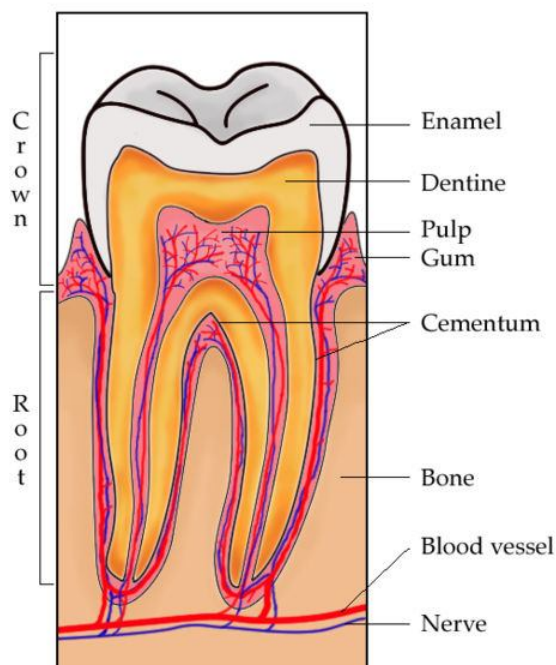


Figure 5.6 Cross section of human tooth [71].

By employing the CPCF delivery, a stack of combined TPEF/SHG images of human tooth are acquired sequentially. The interconnected enamel rods are clearly observed in Fig. 5.7(a)-(b). The wide-band filter used leads to the leakage of TPEF signals into SHG channel, which causes our images to be yellow color. Figure 5.7(c) shows the dentin-enamel junction (DEJ). The enamel rods are in red, the collagens are in green, and the dark holes are in scattered distribution. The dark areas possibly arise from the reduced mineralization. In Fig. 5.7(d)-(f), the fine structure of dentin tubules are clearly revealed by tiny dark tubules in the bright SHG background. As we image deeper, we approach the pulp cavity. Noticeably, the size of dentin tubules gradually increases at greater depth, which matches with the structure of tooth.

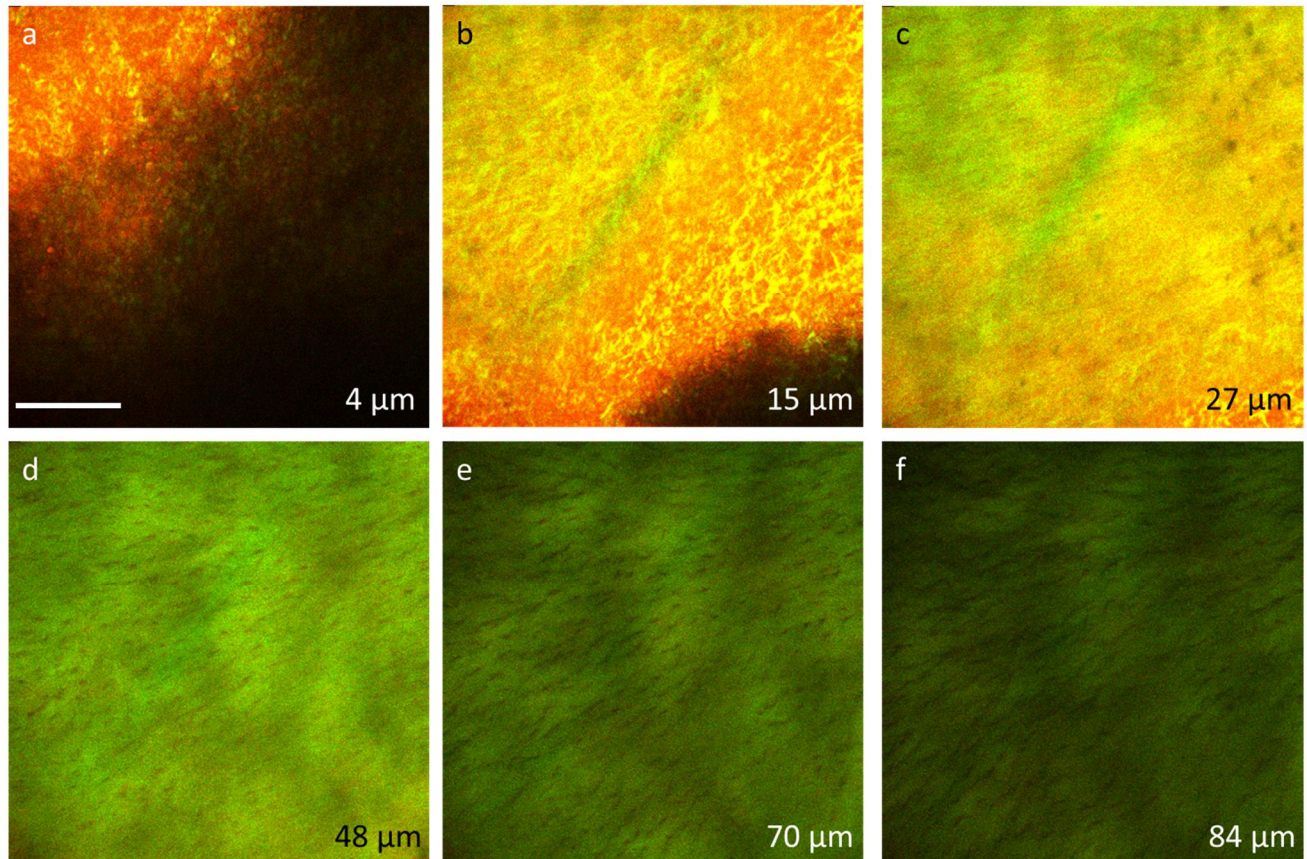


Figure 5.7 MPM images of human tooth at different depths when power delivered by 0.8 m CPCF on the sample is 5 mw; The number on each image denotes the distance of current image from the top surface. Integration time per pixel for all images is 10 μ s. The scale bar is 50 μ m.

For the HC-800-01 delivered illumination, the structures of human tooth are shown in Fig. 5.8. The pixel dwell time is extended to 30 μ s and illuminated power remains the same as with the CPCF delivery. TPEF signals from the enamel in Fig. 5.8(a)-(b) reveal the parallel enamel rods. In Fig. 5.8(c), DEJ is shown by green collagen signals and red enamel signals. At the depth of 48 μ m, the weak signals, arising from dentin, lead to hardly distinguished dentin tubules [Fig. 5.8(d)]. Nevertheless, the signals are much weaker than the case with the CPCF fiber delivery.

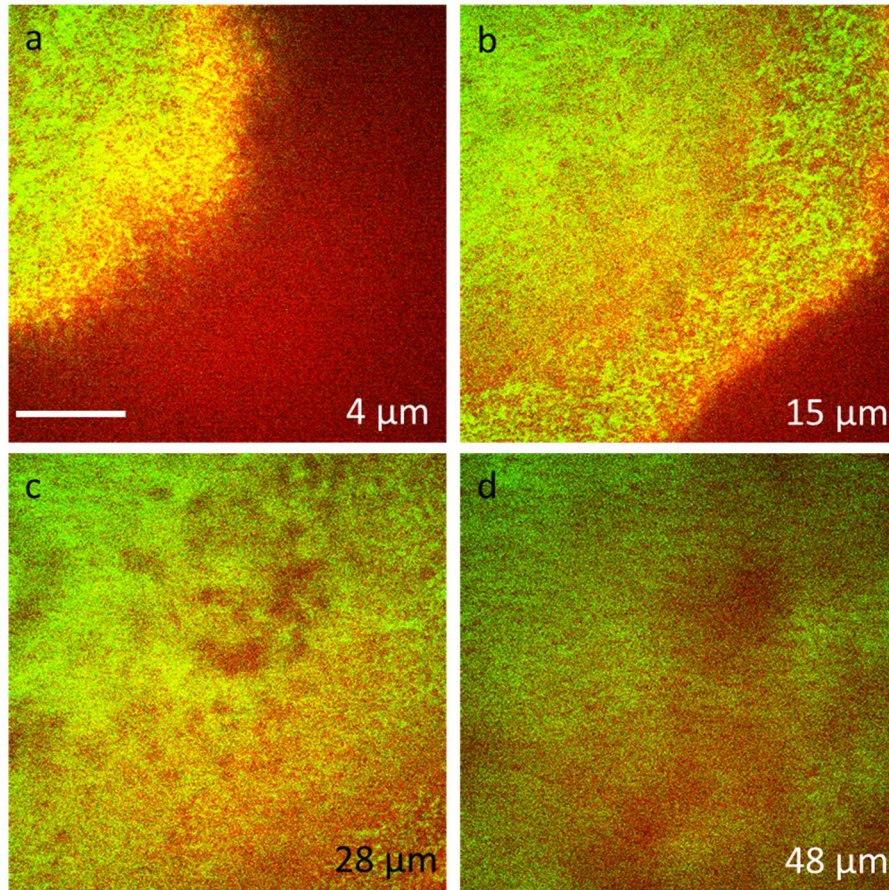


Figure 5.8 MPM images of human tooth when power delivered by the 0.4 m HC-800-01 on the sample is 5 mw and integration time per pixel is 30 μ s. The scale bar is 50 μ m.

5.1.3 Imaging fish cornea with system through light delivered by the CPCF and free space microscopy system

As shown in Fig. 5.9, cornea is comprised of five distinct layers: epithelium, Bowman's layer, stroma, Descemet's membrane, and endothelium. The corneal epithelium is a thin multicellular layer. The tough Bowman's membrane, underneath corneal epithelium, is primarily composed of type I collagen fibers. Corneal stroma, as the thickest layer, is made up of mainly type I collagen with sporadic cells called keratocytes. The Descemet's membrane consists of

type IV collagen fibers. The monolayer of cells at the bottom is endothelium. In order to distinguish the fine structures inside the cornea for the disease diagnosis and surgery guidance, MPM imaging becomes a powerful modality [72, 73].

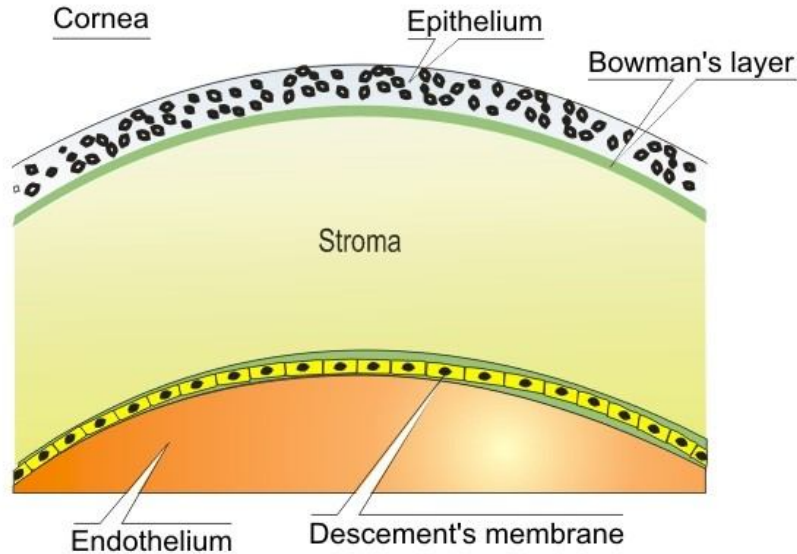


Figure 5.9 Anatomy of the cornea [74].

Using the CPCF-delivery, the representative TPEF and SHG images of a fish cornea are shown from the anterior to the posterior layer in Fig. 5.10. We can see images even though the power delivered through the CPCF on the sample is $\sim 4\text{mW}$. The cells in Fig. 5.10(a) correspond to the epithelium layer. The TPEF signals, from the autofluorescence in cells, combination with SHG signals, from collagen fibers, suggest the boundary between the epithelium and the Bowman's layer [Fig. 5.10(b)]. The direction of collagen fibrils alters in Fig. 5.10(c)-(d), which possibly indicates different sub-layers in the corneal stroma. Due to low illumination power, the endothelium is not observed in the image stacks. By flipping the fish cornea, light propagates from the posterior layer to the anterior layer. Then the similar images distributed with spherical cells in endothelium can be obtained.

In comparison, the MPM images of a fish cornea are acquired at same power on the sample based on free-space microscopy. It is worth mentioning that fish cornea used for free-space microscopy is not exact same one used in CPCF delivery system, but similar type. As shown in Fig. 5.11, the cells in epithelium layer and collagen fibers in corneal stroma are clearly identified. The image quality and image intensity are similar with those obtained by the CPCF-delivery system. Therefore, we think that a piece of CPCF can replace the free space transmission and have comparable MPM images as free space microscopy.

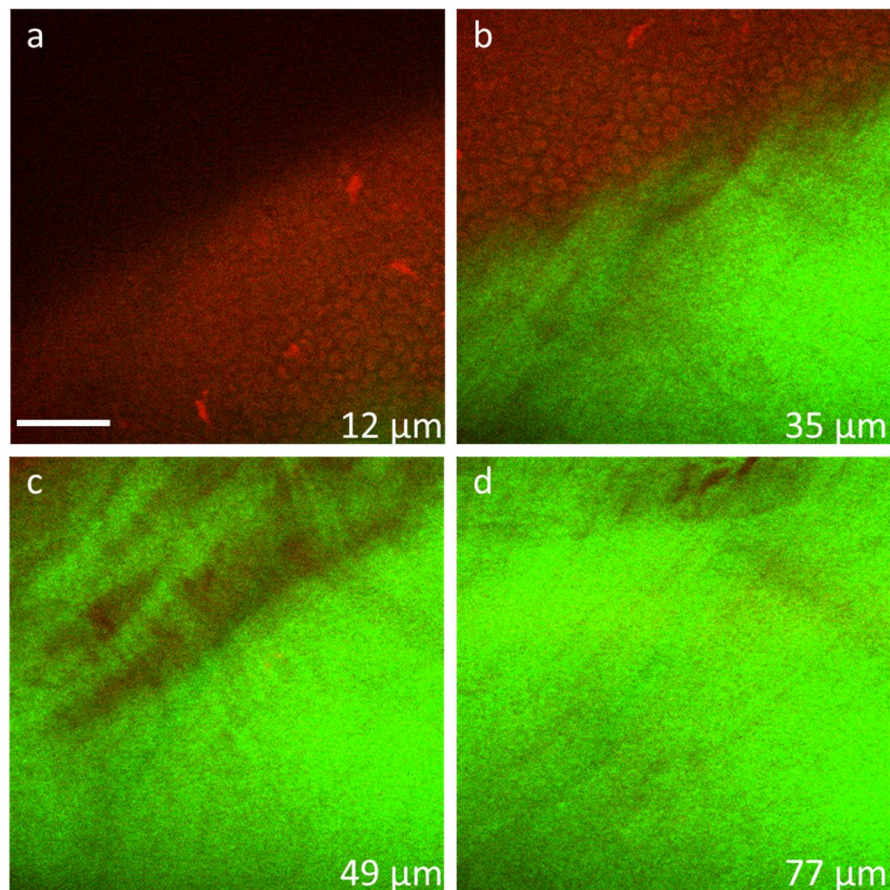


Figure 5.10 MPM images of fish cornea at different depths when power delivered by 0.8 m CPCF on the sample is 4 mw; The number on each image denotes the distance of current image from the top surface. Integration time per pixel for all images is 60 μ s. The scale bar is 50 μ m.

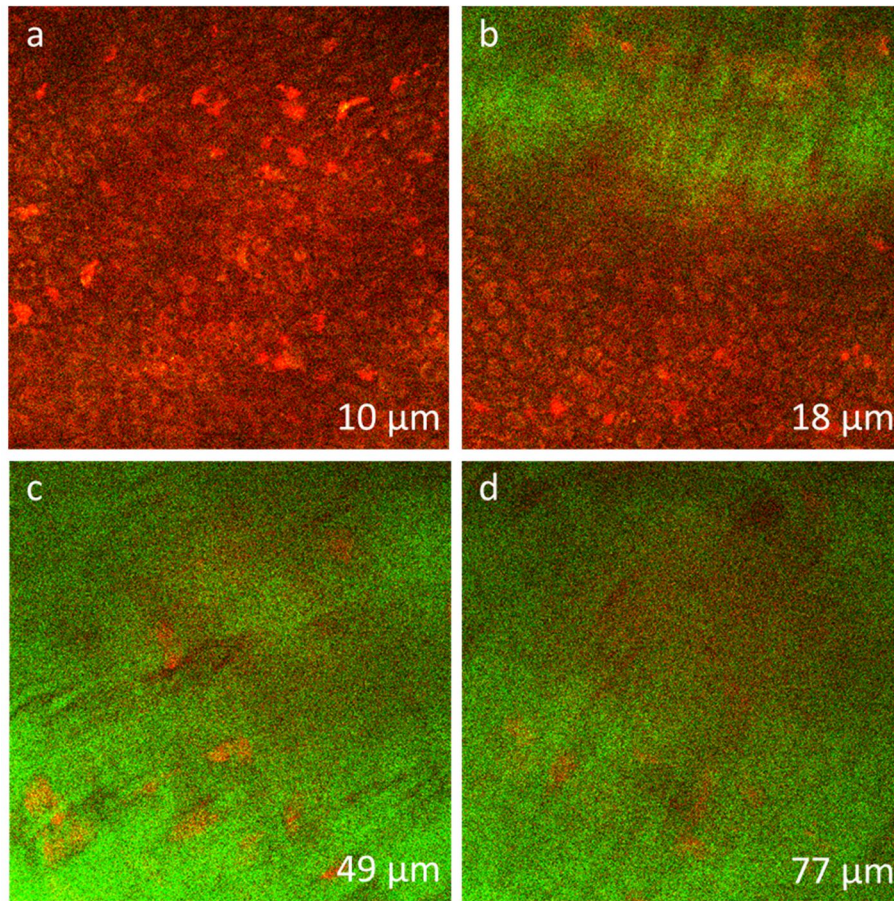


Figure 5.11 MPM images of fish cornea at different depths when power on sample is 4 mW in the free-space microscopy system. The number on each image denotes the depth of current image from the top surface. Integration time per pixel for all images is 30 μ s. The scale bar is 50 μ m.

5.2 Quantitative comparison of image intensities obtained by the two types of fibers

It is evident that all the images acquired with the CPCF delivery provide better contrast than those by the HC-800-01 delivery. For a quantitative comparison, standard samples are used to exclude the cross-talk between the two channels. Fluorescent beads are employed to calibrate the TPEF channel while fish scale is used to calibrate the SHG channel. Nevertheless, the effect

of sample non-uniformity in the intensities should be taken into account. Thus, the TPEF or SGH signal strength is denoted by the average value of the brightest 20% of the pixels of each image.

5.2.1 Calibration by fluorescent beads images and fish scale

The imaging illumination power on the fluorescent beads is kept the same for the two fiber-delivery configurations. Moreover, pixel dwell time of each image and the gain setting in PMT remain unchanged. Furthermore, identical imaging location of fluorescent beads are found to form approximate co-registered images. As shown in Fig. 5.12, the top row of images of fluorescent beads are acquired by the CPCF delivery while those in the bottom row are acquired by HC-800-01 delivery. The black-and-white images are raw data [Fig. 5.12(b), (d), (f), (h)] for direct comparison of absolute signal intensity, whereas the false color images are normalized and enhanced [Fig. 5.12(a), (c), (e), (g)] for better visualization of the structure. Since fluorescent beads have very strong TPEF signals, very low power is applied on the beads to avoid photobleaching. For instance, power of approximately 0.06 mW illuminates on the beads in Figs. 5.12(a), (b), (e), (f). In contrast, the power is doubled in Figs. 5.12(c), (d), (g), and (h). The TPEF intensities are summarized in Table 5.1.

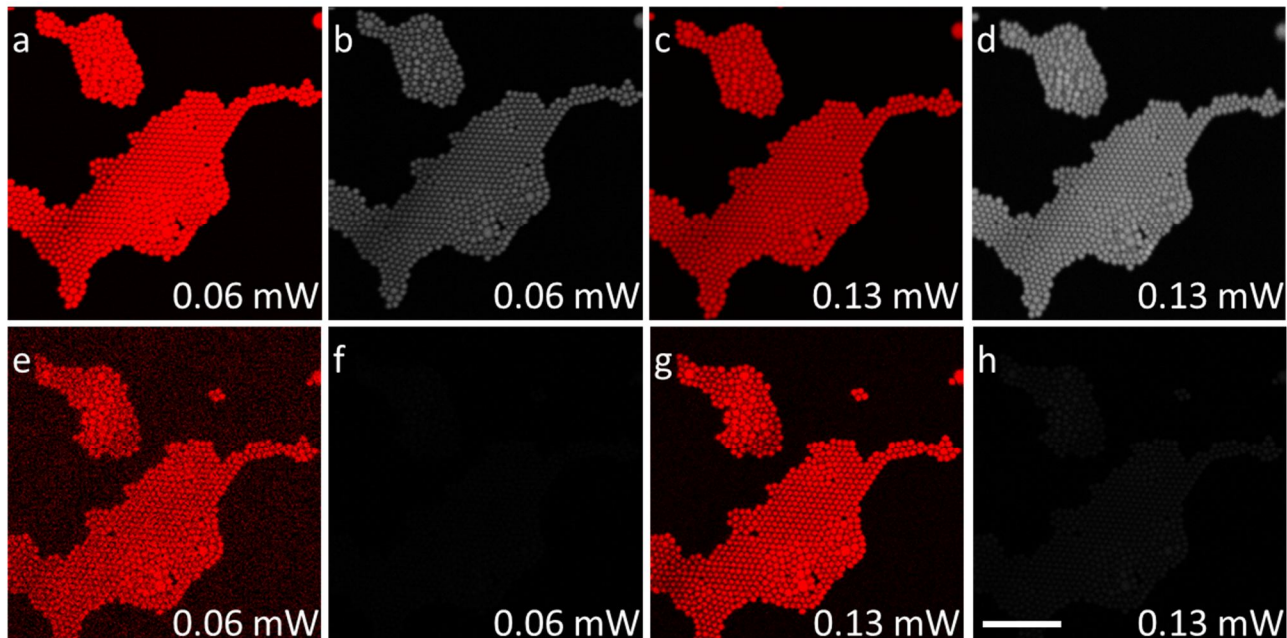


Figure 5.12 TPEF images of fluorescent beads at same imaging condition for the 0.8 m CPCF and 0.4 m HC-800-01 by varied the illumination power on the sample. The above row shows images delivered by CPCF whereas the bottom rows denote images delivered by HC-800-01. The black-white images are raw data [Fig. 5.11(b), (d), (f), (h)] whereas false color images are normalized and enhanced [Fig. 5.11(a), (c), (e), (g)] for direct visualization. The numbers on the right corner of each image signify the illuminated power on the beads. Pixel integration time for all images is 10 μ s. The scale bar is 25 μ m.

Similarly, a piece of fish scale is also imaged because the regularly repeated structure of fish scale provides good SHG contrast. The power on the fish scale is \sim 4 mW for the two fiber-delivered configurations. The pixel dwell time for the CPCF delivery system is 10 μ s whereas pixel dwell time for the HC-800-01 delivery system is 30 μ s. The co-registered SHG images are displayed and analyzed in the same way as the TPEF images of fluorescent beads [Fig. 5.13]. The images in the top row are acquired by the CPCF delivery while those in the bottom row are acquired by HC-800-01 delivery. Two different locations on fish scale are imaged to alleviate the

sample inhomogeneity that may cause the variation of SHG strength. The SHG intensities are summarized in Table 5.1.

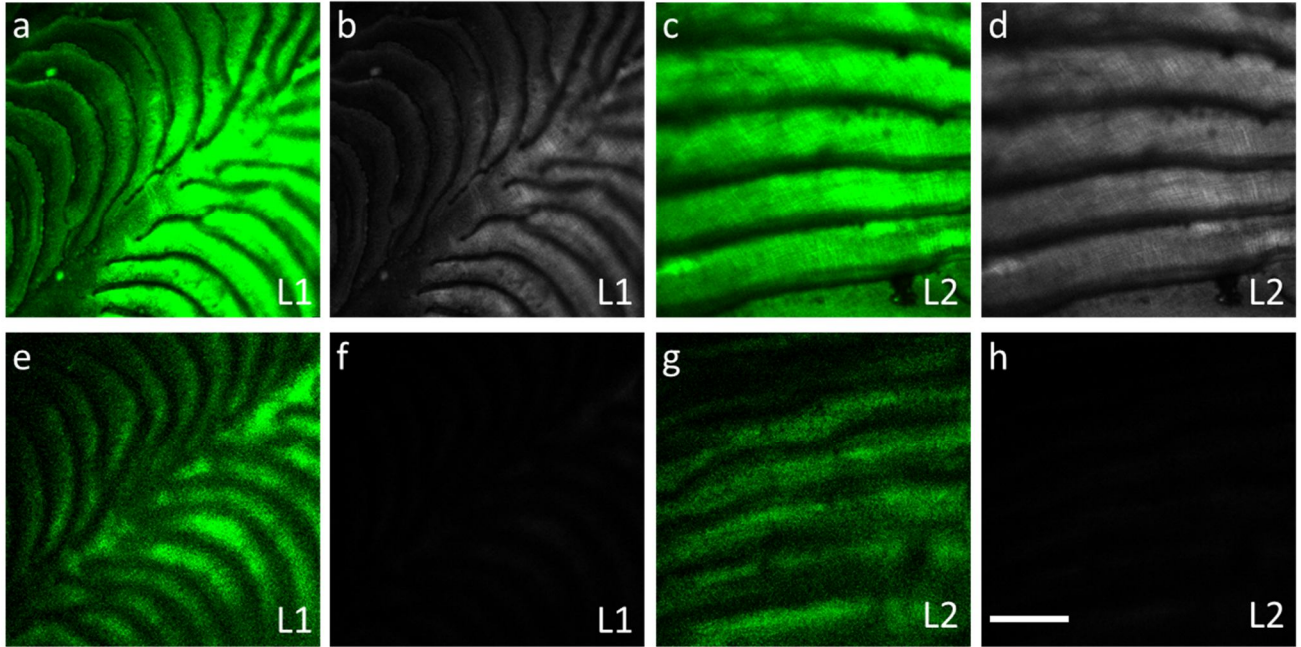


Figure 5.13 SHG images of fish scale at same imaging condition for the 0.8 m CPCF and 0.4 m HC-800-01. The above row shows images delivered by CPCF whereas the bottom rows denote images delivered by HC-800-01. The black-white images are raw data [Fig. 5.11(b), (d), (f), (h)] whereas false color images are normalized and enhanced [Fig. 5.11(a), (c), (e), (g)] for direct visualization. The symbol on the right corner of each image denotes the location one and location two. The scale bar is 50 μm .

We analyzed the above TPEF images of fluorescent beads and SHG images of fish scale in the following two methods. Method I: The average intensity of the 512 X 512 raw image can be obtained by dividing the sum of all pixel intensities by the total number of pixels.

$$I_{avg} = \frac{\sum_{x=1}^{512} \sum_{y=1}^{512} I_{pixel(x,y)}}{512 * 512} \quad (5.1)$$

Using (5.1), we calculate the average intensities of similar images acquired by each fiber-delivery system. Then the ratio of average intensity is defined by

$$Ratio_{avg} = \frac{I_{avg}^{CPCF}}{I_{avg}^{HC-800-01}} \quad (5.2)$$

Method II: Firstly, the intensity histogram of each image (512*512 pixels) is calculated. Then, the brightest 20% pixels are sorted based on their intensities and the average intensities of these pixels are calculated for each image. Finally, we can obtain the ratio of the brightest 20% pixel intensities between the two fiber-delivery systems.

$$I_{20\%} = \frac{\sum_{x=1}^i \sum_{y=1}^j I_{pixel(x,y)}^{brighter}}{i * j}, i * j \leq 512 * 512 * 0.2 \quad (5.3)$$

$$Ratio_{20\%} = \frac{I_{20\%}^{CPCF}}{I_{20\%}^{HC-800-01}} \quad (5.4)$$

The results are summarized in Table 5.1. Comparing CPCF to HCF, our data indicate an enhancement factor of roughly 17 and 56 for TPEF and SHG, respectively.

The enhancement is mainly contributed by the shorter duration of the pulses delivered by the CPCF compared to the pulses delivered by the HC-800-01. From Eq. 1.2 and 1.3, the TPEF and SHG intensities scale with $1/\tau_p$. As shown in Fig.4.6 and Fig. 4.9, the pulse delivered by the 0.8 m CPCF is ~ 20 fs on the specimen plane while the pulse delivered by the 0.4 m HC-800-01 is ~700 fs. If the $1/\tau_p$ relationship is strictly observed, the improvement of image intensities is estimated to be ~35 times as the CPCF provides 35 times shorter pulses at the sample location than HC-800-01. Here, errors may appear on the calculated values of the pulse durations and their ratio since the real pulse shapes may not be exactly the same as the assumed shape (i.e., Hyperbolic secant shape). We demonstrate that the ratio of pulse duration is close to the ratio obtained from analyzing the images.

Furthermore, the enhancement in the TPEF (~17 times) is less than that in the SHG (~56 times). Our results are consistent with previous publications that characterized TPEF dependence on pulse duration [75]. One possible explanation is that the bandwidth of the ultrashort pulses could become broader than the two-photon absorption window of the fluorophore. Therefore, the two-photon absorption efficiency will not further increase if the excitation pulse bandwidth is broader than the absorption bandwidth of the fluorophore, which eventually limits the improvement of TPEF intensities. For SHG, the enhancement is not much limited by the bandwidth of the pulses since SHG is not dependent on absorption. The slight difference between the SHG intensity ratio and the pulsewidth ratio can be caused by two possible reasons. Firstly, a 20 nm broader bandwidth is enabled by the CPCF as compared to the HCF. As a result, the excitation spectra could be improved because phase-matching constraint is not critical for SHG over the microscopy length scale (i.e., focal depths < 20 μm). Secondly, the polarization direction of the light is different after the CPCF and HC-800-01 delivery. Since SHG intensities are sensitive to the polarization direction of incident light, different polarization after the two fiber transmission could lead to different SHG intensities.

Table 5.1 The intensities of fluorescent beads and fish scale for two fiber-delivered systems and corresponding enhancement

Intensities of images	CPCF	HC-800-01	Ratio _{avg}	Ratio _{20%}
Location 1 in fluorescent beads	I _{avg} : 18.52 I _{20%} : 64.96	I _{avg} :1.24 I _{20%} : 3.126	14.77	20.78
Location 2 in fluorescent beads	I _{avg} :42.2 I _{20%} : 141.5	I _{avg} :3.1 I _{20%} : 10.18	13.9	13.9
Location 1 in Fish scale	I _{avg} :45.885 I _{20%} : 80.99	I _{avg} :1.95 I _{20%} : 4.512	69.2	53.85
Location 2 in Fish scale	I _{avg} :57.9 I _{20%} : 100.9	I _{avg} :2.1 I _{20%} : 5.164	82.7	58.6

5.2.2 Comparison for dermis layer in human skin

Skin is used for the comparison because multiple endogenous markers found in the dermis can provide MPM contrasts without staining. Specifically, collagen fibers can provide SHG contrast and elastin fibers can provide TPEF contrast. The side view of a skin dermis layer is imaged by the two fiber configurations.

Figure 5.14 shows the representative MPM images of dermis layer for the CPCF delivery. A stack of images are acquired for different depths to ameliorate the sample dependence and random noise. The power delivered by the CPCF on the fresh skin sample is about 5 mW and the pixel dwell time is 10 μ s. The black-white images [Fig. 5.14(b), (c), (e), (f)] are raw data that show the absolute intensities from TPEF and SHG, separately. The combined images in false

color are enhanced for better visualization of the structures [Fig. 5.14(a), (d)]. Fig. 5.14(a) and Fig. 5.14(d) show two different locations. Based on anatomical features of skin structure, thick collagen bundles and thin elastin fibers are clearly distinguished in Figs. 5.14(a) and (d).

Another piece of skin sample is prepared in the same way since the first piece used in the CPCF-delivered system degrades after one whole day imaging. Under the identical illumination power but longer pixel dwell time (i.e., 30 μ s), the representative MPM images of dermis layer with the HC-800-01 delivery are shown in Fig. 5.15. The images are arranged in the same way as in Fig. 5.14. Fig 5.15 also shows two different locations.

For a fair comparison, we processed the raw images to obtain the average value and average value of the brightest 20% of the pixels of each image. Five different images, indicating five locations in the skin, are selected to make a further average. After removing the highest and lowest values from the five data sets, the ratios of image intensities can be averaged between two fiber-delivery configurations. We observe an enhancement factor of 9 and 46 for the TPEF channel and SHG channel. These data follow similar trend with those acquired by the separate calibration of each channel, even though the origins of MPM contrasts of the human skin are totally different from the fluorescent beads and fish scale. For the three samples, TPEF and SHG signals are significantly enhanced by using CPCF over HC-800-01. This repeatability demonstrates the appealing performance of the CPCF applied in the MPM field.

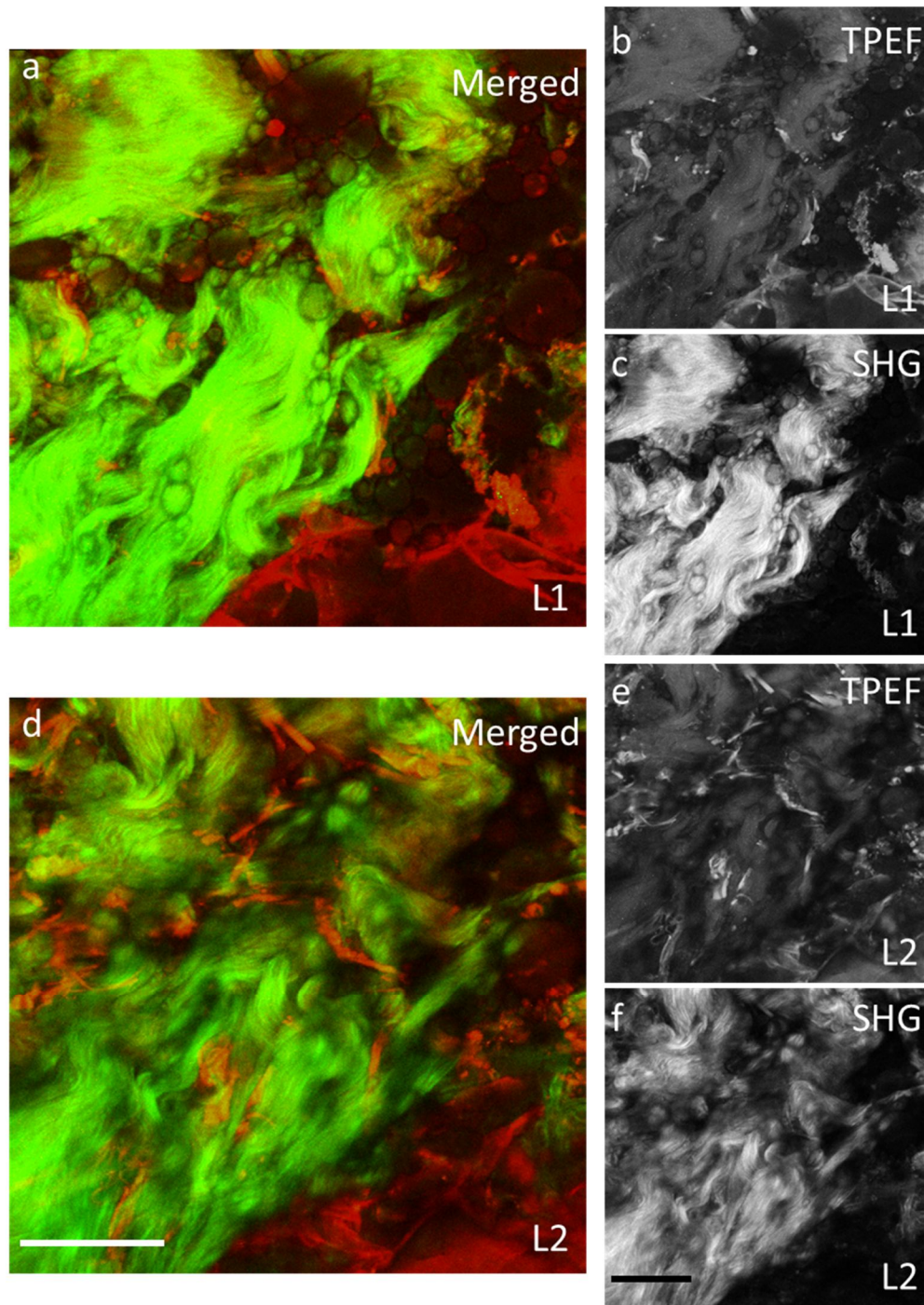


Figure 5.14 Images of the dermis layer of human skin using CPCF with 0.8 m length; Images on left side are combination of TPEF/SHG while images on right hand are obtained from respective single channel. The symbol on the right corner of each image denotes the corresponding location. Pixel dwell time is 10 μ s. The Scale bar is 50 μ m.

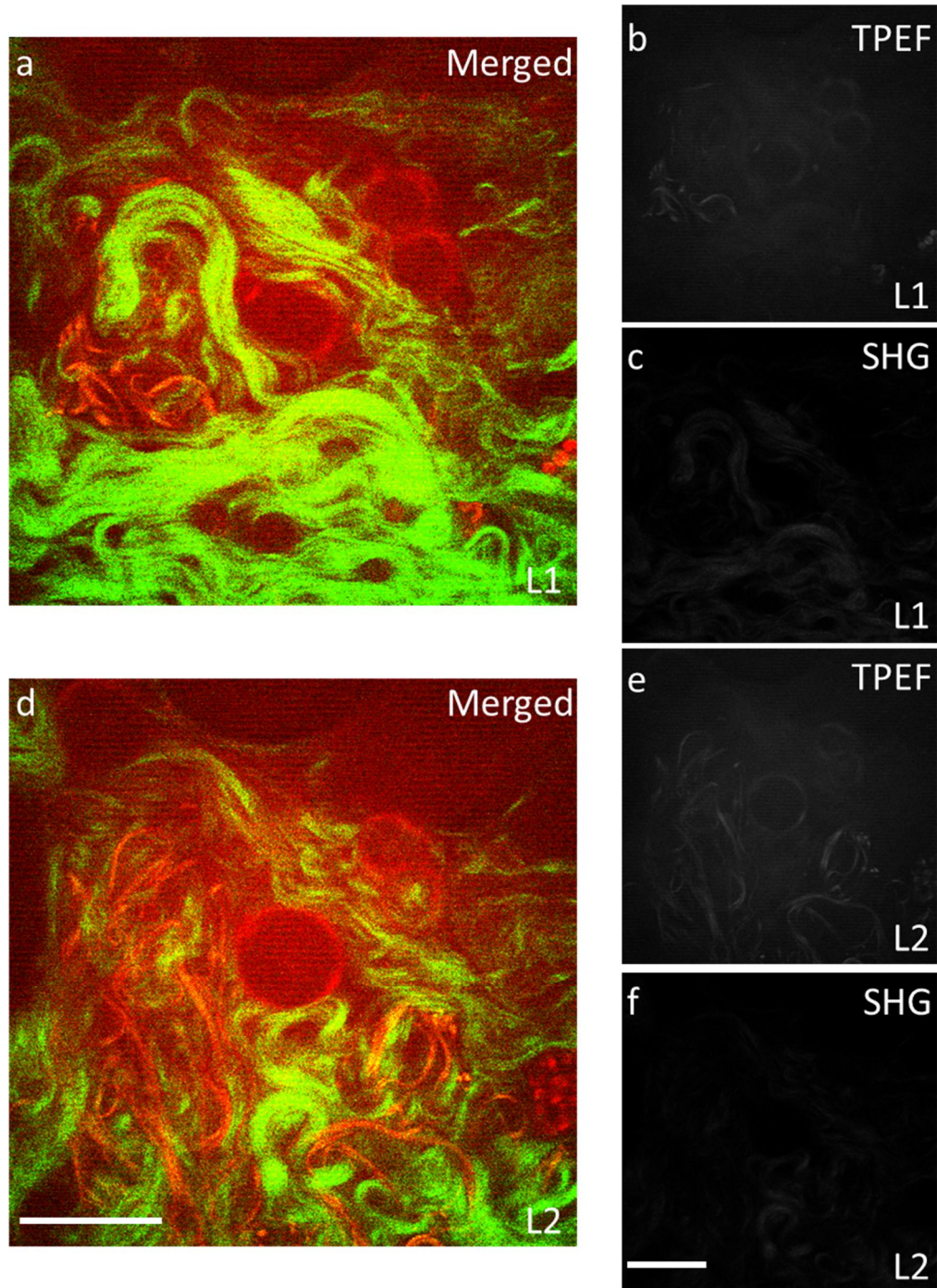


Figure 5.15 cross-section images of the dermis layer of human skin using the HC-800-01 with 0.4 m length; Images on left side are combination of TPEF/SHG while images on right hand are obtained from respective single channel. The location is indicated by the symbol of right corner on each image. Pixel dwell time is 30 μ s. The Scale bar is 50 μ m.

Table 5.2 The intensities of human skin in five locations for two fiber-delivery configurations and the corresponding enhancement

Location of skin	CPCF		HC-800-01		Ratio _{avg}		Ratio _{20%}	
	TPEF	SHG	TPEF	SHG	TPEF	SHG	TPEF	SHG
1	I _{avg} :58.8	I _{avg} :96.7	I _{avg} :20	I _{avg} :4.89	8.8	59.4	9.78	45.3
	I _{20%} :100.2	I _{20%} :212.3	I _{20%} :30.7	I _{20%} :14.1				
2	I _{avg} :60.6	I _{avg} :99.1	I _{avg} :20.2	I _{avg} :5.83	9	51	10.1	38
	I _{20%} :104.2	I _{20%} :211	I _{20%} :30.8	I _{20%} :16.6				
3	I _{avg} :58.4	I _{avg} :90.9	I _{avg} :21	I _{avg} :5.76	8.35	57.3	9.15	45
	I _{20%} :102.2	I _{20%} :192.9	I _{20%} :33.5	I _{20%} :12.9				
4	I _{avg} :50.5	I _{avg} :71.55	I _{avg} :21.8	I _{avg} :3.29	6.96	65.2	8.2	49.7
	I _{20%} :93.78	I _{20%} :153.5	I _{20%} :34.3	I _{20%} :9.25				
5	I _{avg} :44.1	I _{avg} :58.1	I _{avg} :20.75	I _{avg} :2.22	6.37	78.4	7.92	61
	I _{20%} :84.27	I _{20%} :122.2	I _{20%} :31.9	I _{20%} :6.01				
Average after removing max and min					8	60.6	9	46.67

Chapter 6: Conclusion

6.1 Conclusions

A novel photonic crystal fiber with a radically chirped microstructured cladding has been introduced into the multiphoton field. The CPCF is experimentally characterized from several aspects such as NA, spatial mode profile, spectrum, and dispersion. Particularly, dispersion performances under various cases are measured to achieve sub-30 fs pulse after 0.8 m CPCF propagation at the specimen plane. In CPCF-delivered system, the dispersion pre-compensation is only used to balance the normal dispersion from the optical lenses. Comparing CPCF to HC-800-01, CPCF presents extremely low dispersion over an extended bandwidth towards short wavelength. The feasibility of applying CPCF into MPM imaging is demonstrated on various biological samples such as leaf, skin, cornea, and so on. In comparison, the images acquired with the 0.4 m HC-800-01 delivery are shown for similar locations in the identical samples. The MPM images obtained by CPCF and HCF are qualitatively compared and further quantitatively analyzed. Our results show a dramatic increase of the MPM intensities for all images delivered by the 0.8 m CPCF. However, the enhancement factors for TPEF and SHG do not exactly accord with the $1/\tau_P$ relationship between pulsewidth and TPEF/SHG signal strength (~35 times). In details, we observe a roughly 9 times increase for TPEF images and a roughly 45 times increase for SHG images. We refer the limited TPEF improvement to the signal saturation arising from relatively narrow absorption spectrum for the specific fluorophores. For the slightly larger SHG enhancement, the possible explanations are extended excitation bandwidth enabled by the CPCF and polarization direction near optimal angle. In conclusion, CPCF offers a good choice for fiber-based multiphoton endoscopes for increasing the MPM excitation efficiency.

6.2 Future work

In view of great potential of the application of the CPCF in MPM endoscopes, its performances should be further improved in terms of loss and fragility. Firstly, the current loss (~ 5 dB/m) is still high when laser power is limited, which limits the maximum length of the CPCF that can be used. This attenuation could be reduced if the fiber parameters can be optimized for our operating wavelength. Secondly, the CPCF is made of soft glass without any protection layer. Therefore, the CPCF is extremely fragile and difficult to handle. Possibly, the protection layer could be added in later version.

Moreover, the prism-based pre-compensation unit should be further aligned carefully to improve its performance. However, prism stretcher cannot compensate residual higher-order dispersion from the optical lenses and prism itself, which restricts the shortest pulse attained on the sample plane. If highly-dispersive chirped mirrors or MIIPS pulse shaper can be used, sub-20 fs pulse on the focal plane can be obtained and may further increase the MPM excitation efficiency.

In addition, the CPCF could be employed in a tunable laser system to obtain ultrashort pulse delivery over a wide wavelength tuning range. Typically, tunable laser can operate at the range from 720 nm to 1000 nm with pulse duration of ~ 100 fs. One advantage is that the extended spectral range towards the shorter wavelengths could be beneficial for exciting intrinsic fluorophores. Another advantage could be extremely low dispersion over wide bandwidth that is favorable for selective TPEF excitation without the pre-compensation.

In this paragraph, we give some suggestions of MPM endoscope design. As shown in Fig. 6.1, the MPM endoscope can be designed by the CPCF illumination and MMF collection. After

CPCF delivery, the parallel beam is scanned by MEMS scanner or piezoelectric scanner in order to reduce the size. Depending on the beam size, the beam expander may not be employed in the endoscope design. The small aspherical lens can be used as an objective lens to minimize the spherical and chromatic aberrations. The aspherical lens should have high numerical aperture for high lateral resolution. However, the field of view is controlled by the scanner and aspherical lens. A trade-off exists between field of view and lateral resolution, which should be considered in the design. Then the illumination light and fluorescence signals are separated by a dichroic mirror with similar performance used in bench-top system. The fluorescence signals can be collected in backward direction by multimode fibers with large core. The core size of multimode fiber is determined by the magnification of aspherical lens and scanning range. Eventually, MPM signals after multimode fiber collection are focused and filtered before entering the PMT. The filter should be carefully chosen based on the spectral band of the signals that are selected. It should be mentioned that the package of PMT is vital to reject the noises from surrounding room-light.

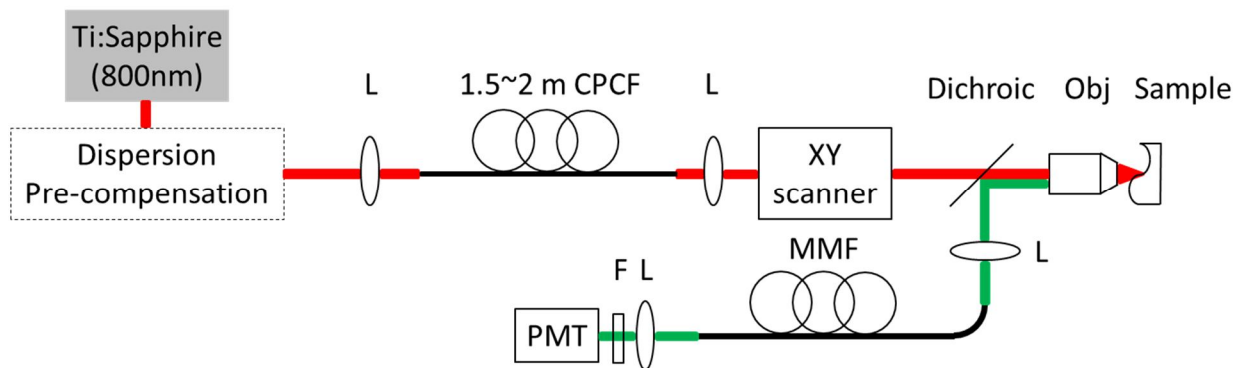


Figure 6.1 Schematic of possible MPM endoscope.

Bibliography

- [1] W. R. Zipfel, R. M. Williams, and W. W. Webb, "Nonlinear magic: multiphoton microscopy in the biosciences," *Nature biotechnology*, vol. 21, pp. 1369-1377, 2003.
- [2] A. Zoumi, A. Yeh, and B. J. Tromberg, "Imaging cells and extracellular matrix in vivo by using second-harmonic generation and two-photon excited fluorescence," *Proceedings of the National Academy of Sciences*, vol. 99, pp. 11014-11019, 2002.
- [3] C. Stosiek, O. Garaschuk, K. Holthoff, and A. Konnerth, "In vivo two-photon calcium imaging of neuronal networks," *Proceedings of the National Academy of Sciences*, vol. 100, pp. 7319-7324, 2003.
- [4] C. R. Rose, Y. Kovalchuk, J. Eilers, and A. Konnerth, "Two-photon Na⁺ imaging in spines and fine dendrites of central neurons," *Pflügers Archiv*, vol. 439, pp. 201-207, 1999.
- [5] D. A. Dombeck, K. A. Kasischke, H. D. Vishwasrao, M. Ingelsson, B. T. Hyman, and W. W. Webb, "Uniform polarity microtubule assemblies imaged in native brain tissue by second-harmonic generation microscopy," *Proceedings of the National Academy of Sciences*, vol. 100, pp. 7081-7086, 2003.
- [6] E. B. Brown, R. B. Campbell, Y. Tsuzuki, L. Xu, P. Carmeliet, D. Fukumura, *et al.*, "In vivo measurement of gene expression, angiogenesis and physiological function in tumors using multiphoton laser scanning microscopy," *Nature medicine*, vol. 7, pp. 864-868, 2001.
- [7] W. Wang, J. B. Wyckoff, V. C. Frohlich, Y. Oleynikov, S. Hüttelmaier, J. Zavadil, *et al.*, "Single cell behavior in metastatic primary mammary tumors correlated with gene expression patterns revealed by molecular profiling," *Cancer research*, vol. 62, pp. 6278-6288, 2002.
- [8] W. Denk, J. H. Strickler, and W. W. Webb, "Two-photon laser scanning fluorescence microscopy," *Science*, vol. 248, pp. 73-76, 1990.
- [9] P. J. Campagnola, M. Wei, A. Lewis, and L. M. Loew, "High-resolution nonlinear optical imaging of live cells by second harmonic generation," *Biophysical journal*, vol. 77, p. 3341, 1999.
- [10] P. J. Campagnola and L. M. Loew, "Second-harmonic imaging microscopy for visualizing biomolecular arrays in cells, tissues and organisms," *Nature biotechnology*, vol. 21, pp. 1356-1360, 2003.
- [11] N. S. Claxton, T. J. Fellers, and M. W. Davidson, "Laser scanning confocal microscopy," *Olympus*. Available online at <http://www.olympusconfocal.com/theory/LSCMIntro.pdf>, 2006.
- [12] J. B. Pawley, *Handbook of biological confocal microscopy*: Kluwer Academic Publishers, 1995.
- [13] F. Helmchen and W. Denk, "Deep tissue two-photon microscopy," *Nature methods*, vol. 2, pp. 932-940, 2005.
- [14] S. J. Mulligan, B. A. MacVicar, A. Méndez-Vilas, and J. Díaz, "Two-photon fluorescence microscopy: basic principles, advantages and risks," *Modern Research and Educational Topics in Microscopy*, A. Méndez-Vilas, and J. Díaz, eds.(FORMATEX, Badajoz, Spain, 2007), pp. 881-889, 2007.

- [15] P. T. So, C. Y. Dong, B. R. Masters, and K. M. Berland, "Two-photon excitation fluorescence microscopy," *Annual review of biomedical engineering*, vol. 2, pp. 399-429, 2000.
- [16] W. R. Zipfel, R. M. Williams, R. Christie, A. Y. Nikitin, B. T. Hyman, and W. W. Webb, "Live tissue intrinsic emission microscopy using multiphoton-excited native fluorescence and second harmonic generation," *Proceedings of the National Academy of Sciences*, vol. 100, pp. 7075-7080, 2003.
- [17] S. Mironov and D. Richter, "Oscillations and hypoxic changes of mitochondrial variables in neurons of the brainstem respiratory centre of mice," *The Journal of physiology*, vol. 533, pp. 227-236, 2001.
- [18] P. J. Campagnola, A. C. Millard, M. Terasaki, P. E. Hoppe, C. J. Malone, and W. A. Mohler, "Three-dimensional high-resolution second-harmonic generation imaging of endogenous structural proteins in biological tissues," *Biophysical journal*, vol. 82, p. 493, 2002.
- [19] S. Jaisson, S. Lorimier, S. Ricard-Blum, G. D. Sockalingum, C. Delevallée-Forte, G. Kegelaer, *et al.*, "Impact of carbamylation on type I collagen conformational structure and its ability to activate human polymorphonuclear neutrophils," *Chemistry & biology*, vol. 13, pp. 149-159, 2006.
- [20] P. Campagnola, "Second harmonic generation imaging microscopy: applications to diseases diagnostics," *Analytical chemistry*, vol. 83, pp. 3224-3231, 2011.
- [21] R. Hellwarth and P. Christensen, "Nonlinear optical microscope using second harmonic generation," *Appl. Opt*, vol. 14, pp. 247-248, 1975.
- [22] F. Helmchen, M. S. Fee, D. W. Tank, and W. Denk, "A miniature head-mounted two-photon microscope: high-resolution brain imaging in freely moving animals," *Neuron*, vol. 31, pp. 903-912, 2001.
- [23] C. L. Hoy, N. J. Durr, P. Chen, W. Piyawattanametha, H. Ra, O. Solgaard, *et al.*, "Miniaturized probe for femtosecond laser microsurgery and two-photon imaging," *Optics express*, vol. 16, p. 9996, 2008.
- [24] B. A. Flusberg, E. D. Cocker, W. Piyawattanametha, J. C. Jung, E. L. Cheung, and M. J. Schnitzer, "Fiber-optic fluorescence imaging," *Nature Methods*, vol. 2, pp. 941-950, 2005.
- [25] L. Fu and M. Gu, "Fibre - optic nonlinear optical microscopy and endoscopy," *Journal of microscopy*, vol. 226, pp. 195-206, 2007.
- [26] D. Bird and M. Gu, "Fibre - optic two - photon scanning fluorescence microscopy," *Journal of microscopy*, vol. 208, pp. 35-48, 2002.
- [27] W. Göbel, J. N. Kerr, A. Nimmerjahn, and F. Helmchen, "Miniaturized two-photon microscope based on a flexible coherent fiber bundle and a gradient-index lens objective," *Optics letters*, vol. 29, pp. 2521-2523, 2004.
- [28] B. A. Flusberg, J. C. Jung, E. D. Cocker, E. P. Anderson, and M. J. Schnitzer, "In vivo brain imaging using a portable 3.9 gram two-photon fluorescence microendoscope," *Optics letters*, vol. 30, pp. 2272-2274, 2005.
- [29] W. Göbel, A. Nimmerjahn, and F. Helmchen, "Distortion-free delivery of nanojoule femtosecond pulses from a Ti: sapphire laser through a hollow-core photonic crystal fiber," *Optics letters*, vol. 29, pp. 1285-1287, 2004.
- [30] M. T. Myaing, D. J. MacDonald, and X. Li, "Fiber-optic scanning two-photon fluorescence endoscope," *Optics letters*, vol. 31, pp. 1076-1078, 2006.

- [31] L. Fu, A. Jain, H. Xie, C. Cranfield, and M. Gu, "Nonlinear optical endoscopy based on a double-clad photonic crystal fiber and a MEMS mirror," *Optics Express*, vol. 14, pp. 1027-1032, 2006.
- [32] S. Tang, W. Jung, D. McCormick, T. Xie, J. Su, Y.-C. Ahn, *et al.*, "Design and implementation of fiber-based multiphoton endoscopy with microelectromechanical systems scanning," *Journal of biomedical optics*, vol. 14, pp. 034005-034005-7, 2009.
- [33] J. S. Skibina, R. Iliew, J. Bethge, M. Bock, D. Fischer, V. I. Beloglasov, *et al.*, "A chirped photonic-crystal fibre," *Nature Photonics*, vol. 2, pp. 679-683, 2008.
- [34] G. P. Agrawal, *Nonlinear fiber optics*: Springer, 2000.
- [35] J.-C. Diels, W. Rudolph, and S. A. Miller, "Ultrashort laser pulse phenomena," *Optical Engineering*, vol. 36, pp. 2362-2362, 1997.
- [36] L. Fu, "Fibre-optic nonlinear optical microscopy and endoscopy," Doctoral PhD, Faculty of Engineering and Industrial Sciences, Swinburne University of Technology, 2007.
- [37] P. Russell, "Photonic crystal fibers," *science*, vol. 299, pp. 358-362, 2003.
- [38] J. C. Knight, "Photonic crystal fibres," *Nature*, vol. 424, pp. 847-851, 2003.
- [39] F. Benabid and F. Couny, "PHOTONIC-CRYSTAL FIBERS: Hollow-core PCFs enable high nonlinearity at low light levels," *Laser Focus World*, vol. 44, 2008.
- [40] P. Russell, "Photonic crystal fiber: finding the holey grail," *Optics and photonics news*, vol. 18, pp. 26-31, 2007.
- [41] F. Benabid, "Hollow-core photonic bandgap fibre: new light guidance for new science and technology," *Philosophical Transactions of the Royal Society A: Mathematical, Physical and Engineering Sciences*, vol. 364, pp. 3439-3462, 2006.
- [42] P. Ghenuche, S. Rammler, N. Y. Joly, M. Scharrer, M. Frosz, J. Wenger, *et al.*, "Kagome hollow-core photonic crystal fiber probe for Raman spectroscopy," *Optics letters*, vol. 37, pp. 4371-4373, 2012.
- [43] D. G. Ouzounov, F. R. Ahmad, D. Müller, N. Venkataraman, M. T. Gallagher, M. G. Thomas, *et al.*, "Generation of megawatt optical solitons in hollow-core photonic band-gap fibers," *Science*, vol. 301, pp. 1702-1704, 2003.
- [44] S.-P. Tai, M.-C. Chan, T.-H. Tsai, S.-H. Guol, L.-J. Chen, and C.-K. Sun, "Two-photon fluorescence microscope with a hollow-core photonic crystal fiber," in *Biomedical Optics 2005*, 2005, pp. 146-153.
- [45] *NKT photonics*. Available: <http://www.nktpotonics.com/files/files/HC-800-01-100409.pdf>
- [46] J. Bethge, G. Steinmeyer, S. Burger, F. Lederer, and R. Iliew, "Guiding properties of chirped photonic crystal fibers," *Journal of Lightwave Technology*, vol. 27, pp. 1698-1706, 2009.
- [47] B. Pal, "Frontiers in Guided Wave Optics and Optoelectronics," *Rijeka, Croatia: InTech*, 2010.
- [48] G. Steinmeyer, "A review of ultrafast optics and optoelectronics," *Journal of Optics A: Pure and Applied Optics*, vol. 5, p. R1, 2003.
- [49] F. Kärtner, N. Matuschek, T. Schibli, U. Keller, H. Haus, C. Heine, *et al.*, "Design and fabrication of double-chirped mirrors," *Optics letters*, vol. 22, pp. 831-833, 1997.
- [50] E. Treacy, "Optical pulse compression with diffraction gratings," *Quantum Electronics, IEEE Journal of*, vol. 5, pp. 454-458, 1969.

- [51] O. Martinez, "3000 times grating compressor with positive group velocity dispersion: Application to fiber compensation in 1.3-1.6 μm region," *Quantum Electronics, IEEE Journal of*, vol. 23, pp. 59-64, 1987.
- [52] R. Fork, O. Martinez, and J. Gordon, "Negative dispersion using pairs of prisms," *Optics letters*, vol. 9, pp. 150-152, 1984.
- [53] M. Müller, J. Squier, R. Wolleschensky, U. Simon, and G. Brakenhoff, "Dispersion pre-compensation of 15 femtosecond optical pulses for high-numerical-aperture objectives," *Journal of microscopy*, vol. 191, pp. 141-150, 1998.
- [54] B. E. Saleh, M. C. Teich, and B. E. Saleh, *Fundamentals of photonics* vol. 22: Wiley New York, 1991.
- [55] D. E. Gray, *American institute of physics handbook*: McGraw-Hill, 1982.
- [56] F. A. Jenkins and H. E. White, "Fundamentals of optics," *New York: McGraw-Hill, 1957, 3rd ed.*, vol. 1, 1957.
- [57] J.-C. M. Diels, J. J. Fontaine, I. C. McMichael, and F. Simoni, "Control and measurement of ultrashort pulse shapes (in amplitude and phase) with femtosecond accuracy," *Applied Optics*, vol. 24, pp. 1270-1282, 1985.
- [58] T. Francis and X. Yang, *Introduction to optical engineering*: Cambridge University Press, 1997.
- [59] Y. Deng, Q. Sun, S. Cao, J. Yu, C.-y. Wang, and Z. Zhang, "Measurement of Ultrashort Optical Pulses."
- [60] J. B. Guild, C. Xu, and W. W. Webb, "Measurement of group delay dispersion of high numerical aperture objective lenses using two-photon excited fluorescence," *Applied optics*, vol. 36, pp. 397-401, 1997.
- [61] A. M. Larson and A. T. Yeh, "Ex vivo characterization of sub-10-fs pulses," *Optics letters*, vol. 31, pp. 1681-1683, 2006.
- [62] Z. Bor and B. Racz, "Group velocity dispersion in prisms and its application to pulse compression and travelling-wave excitation," *Optics communications*, vol. 54, pp. 165-170, 1985.
- [63] J. Kafka and T. Baer, "Prism-pair dispersive delay lines in optical pulse compression," *Optics letters*, vol. 12, pp. 401-403, 1987.
- [64] B. R. Masters and P. T. So, "Confocal microscopy and multi-photon excitation microscopy of human skin in vivo," *Opt. Express*, vol. 8, pp. 2-10, 2001.
- [65] K. Koenig and I. Riemann, "High-resolution multiphoton tomography of human skin with subcellular spatial resolution and picosecond time resolution," *Journal of biomedical optics*, vol. 8, pp. 432-439, 2003.
- [66] A. Lee, H. Wang, Y. Yu, S. Tang, J. Zhao, H. Lui, *et al.*, "< i> In vivo</i> video rate multiphoton microscopy imaging of human skin," *Optics letters*, vol. 36, pp. 2865-2867, 2011.
- [67] M. B. Ericson, C. Simonsson, S. Guldbrand, C. Ljungblad, J. Paoli, and M. Smedh, "Two - photon laser - scanning fluorescence microscopy applied for studies of human skin," *Journal of biophotonics*, vol. 1, pp. 320-330, 2008.
- [68] P.-Y. Lin, H.-C. Lyu, C.-Y. S. Hsu, C.-S. Chang, and F.-J. Kao, "Imaging carious dental tissues with multiphoton fluorescence lifetime imaging microscopy," *Biomedical optics express*, vol. 2, p. 149, 2011.

- [69] S.-Y. Chen, C.-Y. S. Hsu, and C.-K. Sun, "Epi-third and second harmonic generation microscopic imaging of abnormal enamel," *Opt. Express*, vol. 16, pp. 11670-11679, 2008.
- [70] S. Tang, Y. Zhou, and M. J. Ju, "Multimodal optical imaging with multiphoton microscopy and optical coherence tomography," *Journal of Biophotonics*, vol. 5, pp. 396-403, 2012.
- [71] *Cross section of human tooth.* Available: http://en.wikipedia.org/wiki/Tooth_development
- [72] A. T. Yeh, N. Nassif, A. Zoumi, and B. J. Tromberg, "Selective corneal imaging using combined second-harmonic generation and two-photon excited fluorescence," *Optics letters*, vol. 27, pp. 2082-2084, 2002.
- [73] S.-W. Teng, H.-Y. Tan, J.-L. Peng, H.-H. Lin, K. H. Kim, W. Lo, *et al.*, "Multiphoton autofluorescence and second-harmonic generation imaging of the ex vivo porcine eye," *Investigative ophthalmology & visual science*, vol. 47, pp. 1216-1224, 2006.
- [74] *Anatomy of the cornea.* Available: <http://www.medicatravel.co.uk/Ogonkirurgi/4.1.1%20-%20Ogonkirurgi%20-%20Ogats%20anatom%20-%20Hornhinnan.htm>
- [75] S. Tang, T. B. Krasieva, Z. Chen, G. Tempea, and B. J. Tromberg, "Effect of pulse duration on two-photon excited fluorescence and second harmonic generation in nonlinear optical microscopy," *Journal of biomedical optics*, vol. 11, pp. 020501-020501-3, 2006.

Appendix A: Research ethics

The use of human tissues and animal tissues in this thesis is for the purpose of demonstrating the imaging ability of the chirped photonic crystal fiber in multiphoton microscopy. All the samples simply act as objects to be observed. No additional studies were performed on the tissues and no live animals were kept in the lab.

The fish cornea was acquired from the local supermarkets. Therefore, animal ethics is not required.

The human skin was obtained from BC cancer center. And corresponding ethics protocol is H96-70499.

The human tooth was a baby tooth that naturally fell off from an 8 year-old girl. No information or materials inside tooth had identifiers attached to it. The personal opinions are not needed and the privacy is not violated. The human tooth as a bulk was investigated under multiphoton microscopy for imaging. As a case study, ethics approval is not required.